Scrutiny of a very young, metal-poor star-forming Lyα-emitter at z 3.7

E. Iani, A. Zanella, J. Vernet, J. Richard, M. Gronke, F. Arrigoni-Battaia, A. Bolamperti, K. Caputi, A. Humphrey, G. Rodighiero, et al.

Monthly Notices of the ROYAL ASTRONOMICAL SOCIETY

MNRAS **518,** 5018–5035 (2023) https://doi.org/10.1093/mnras/stac3198
Advance Access publication 2022 November 9

Scrutiny of a very young, metal-poor star-forming Lyα emitter at $z \approx 3.7$

E. Iani [1]★ A. Zanella [2] J. Vernet [3] J. Richard [4] M. Gronke [5] F. Arrigoni-Battaia [5] A. Bolamperti,[6] K. I. Caputi,[1] A. Humphrey,[7] G. Rodighiero [6] P. Rinaldi[1] and E. Vanzella[8]

[1]*Kapteyn Astronomical Institute, University of Groningen, NL-9700 AV Groningen, the Netherlands*
[2]*Istituto Nazionale di Astrofisica (INAF), Vicolo dell'Osservatorio 5, I-35122 Padova, Italy*
[3]*European Southern Observatory, Karl-Schwarzschild-Straße 2, D-85748 Garching bei München, Germany*
[4]*Univ. Lyon, Univ Lyon1, ENS de Lyon, CNRS, Centre de Recherche Astrophysique de Lyon UMR5574, F-69230 Saint-Genis-Laval, France*
[5]*Max-Planck-Institut fur Astrophysik, Karl-Schwarzschild-Straße 1, D-85748 Garching bei München, Germany*
[6]*Dipartimento di Fisica ed Astronomia, Università degli Studi di Padova, Vicolo dell'Osservatorio 3, I-35122 Padova, Italy*
[7]*Instituto de Astrofísica e Ciências do Espaço – Centro de Astrofísica da Universidade do Porto, Rua das Estrelas, P-4150-762 Porto, Portugal*
[8]*Istituto Nazionale di Astrofisica (INAF), Osservatorio di Astrofisica e Scienza dello Spazio, via Gobetti 93/3, I-40129 Bologna, Italy*

Accepted 2022 November 2. Received 2022 October 22; in original form 2022 August 3

ABSTRACT

The origin of the Lyman α (Lyα) emission in galaxies is a long-standing issue: despite several processes known to originate this line (e.g. active galactic nucleus, star formation, cold accretion, shock heating), it is difficult to discriminate among these phenomena based on observations. Recent studies have suggested that the comparison of the ultraviolet (UV) and optical properties of these sources could solve the riddle. For this reason, we investigate the rest-frame UV and optical properties of Abell 2895b, a strongly lensed Lyα emitter at redshift $z \sim 3.7$. From this study, we find that our target is a compact ($r_n \sim$ 1.2 pkpc) star-forming (star formation rate $\simeq$11 $M_\odot$ yr^{-1}) galaxy having a young stellar population. Interestingly, we measure a high ratio of the Hβ and the UV continuum monochromatic luminosities (L(Hβ)/L(UV) $\simeq$ 100). Based on tracks of theoretical stellar models (STARBURST99 and BPASS), we can only partially explain this result by assuming a recent ($\lesssim$10 Myr), bursty episode of star formation and considering models characterized by binary stars, a top-heavy initial mass function and subsolar metallicities ($Z \lesssim 0.01\ Z_\odot$). These assumptions also explain the observed low (C/O) abundance of our target ($\simeq$0.23(C/O)$_\odot$). By comparing the UV and optical data sets, we find that the Lyα and UV continuum are more extended ($\times$2) than the Balmer lines, and that the peak of the Lyα is offset ($\simeq$0.6 pkpc). The multiwavelength results of our analysis suggest that the observed Lyα emission originates from a recent star formation burst, likely taking place in an off-centre clump.

Key words: galaxies: evolution – galaxies: high-redshift – galaxies: ISM – galaxies: starburst – galaxies: star formation – ultraviolet: galaxies.

1 INTRODUCTION

In the hydrogen atom, whenever an electron falls from the first excitation level 2p to the ground state 1s, a photon with an energy of 10.2 eV and a wavelength of 1215.67 Å is emitted. This ultraviolet (UV) transition is the brightest hydrogen emission and it is commonly referred to as Lyman α (Lyα) line (Lyman 1906). Thanks to its brightness and the fact that hydrogen constitutes about 74 per cent of the baryonic matter in the Universe (e.g. Croswell 1996; Carroll & Ostlie 2006), the Lyα acts as a beacon for the detection of galaxies at intermediate/high redshifts ($z \gtrsim$ 2–3). In fact, its UV rest-frame wavelength is shifted into the optical and near-infrared (NIR) at cosmological distances (cosmological redshift).

Galaxies detected through their Lyα emission (and having a rest-frame Lyα equivalent width EW$_0 \gtrsim$ 20 Å) are generally referred to as Lyα emitters (LAEs; e.g. Ouchi, Ono & Shibuya 2020). In the last decades, studies have revealed that these systems have often compact morphologies with effective radii $r_e \sim$ 1 pkpc (e.g. Pascarelle et al. 1996; Matthee et al. 2021; Pucha et al. 2022) and, typically, a disc-like radial surface brightness (SB) profile with a Sérsic index of $n_s \sim$ 1 (e.g. Taniguchi et al. 2009; Gronwall et al. 2011). Whenever in the absence of an active galactic nucleus (AGN), LAEs are found to be low-mass (stellar mass $M_\star \sim 10^{7-9}\ M_\odot$), young (stellar ages $\sim$10 Myr) star-forming galaxies (SFGs) with star formation rates SFRs $\sim$ 1–10 $M_\odot$ yr^{-1} (e.g. Nakajima et al. 2012; Hagen et al. 2014, 2016; Matthee et al. 2021; Pucha et al. 2022). With a specific star formation rate sSFR $\gtrsim 10^{-7}$ yr^{-1} (sSFR = SFR/$M_\star$), LAEs are generally starbursting systems. As for the properties of their interstellar medium (ISM), LAEs are dust-poor galaxies with stellar and nebular colour extinction values $E(B-V) \sim$ 0–0.2 (Ono et al. 2010; Kojima et al. 2017), and a gas-phase metallicity (derived from both strong lines and direct electron temperature T_e methods) $Z \sim$ 0.1–0.5 $Z_\odot$ (e.g. Finkelstein et al. 2011; Nakajima et al. 2012; Trainor et al. 2016; Kojima et al. 2017). Despite all these findings, the origin of their Lyα emission is still debated.

Up to date, five major phenomena are generally invoked to explain Lyα emission in and surrounding galaxies (e.g. Ouchi et al. 2020): *in situ* and/or *ex situ* (i.e. from unresolved faint satellite galaxies; e.g. Mas-Ribas et al. 2017) star formation, AGN, shock heating due to

★ E-mail: iani@astro.rug.nl

outflows, cold accretion via gravitational cooling, and fluorescence, i.e. when ionizing photons can escape their production area and reach and ionize pockets of ISM far from star-forming regions. Despite the fact that each one of these processes can originate the Lyα line, the emission observed in galaxies is possibly driven by a combination of phenomena, each one dominant on a different scale (see Claeyssens et al. 2022, and references therein). To discriminate between these different phenomena is, therefore, a demanding task.

Notwithstanding its brightness, the Lyα line is complex to study since it strongly suffers from both dust extinction and resonant scattering. While the main effect of dust is to erode the UV flux and to re-emit it at the infrared (IR) wavelengths, resonant scattering is a diffusive process where Lyα photons do not escape freely from their production site but undergo a number of absorption and remission events due to intervening atoms of neutral hydrogen along the photons propagation line. The amount of scatterings strongly depends on the properties of the medium the Lyα photons diffuse into, i.e. its neutral hydrogen column density, geometry, and kinematics (see e.g. Dijkstra 2014, and references therein). Besides, each scattering slightly alters the frequency of the Lyα photons, as well as their direction of propagation (Osterbrock 1962). Hence, the spectral characteristics of the emerging radiation (i.e. the spectral shape of the observed Lyα) do not only encode the properties of the phenomena driving the emission of the line but also those of the scattering medium along the paths that offered least resistance to the diffusing photons (e.g. Dijkstra, Gronke & Sobral 2016; Gronke & Dijkstra 2016). This makes observationally challenging determining what are the actual processes driving the Lyα emission.

A potential way to tackle this problem is to investigate in depth the properties of the host galaxy and its surrounding medium, and possibly, spatially resolve them. In particular, the joint analysis of the SB profiles and spatial extent of optical hydrogen transitions (i.e. the Balmer lines), Lyα and UV stellar continuum are believed to be a useful tool to disentangle the different scenarios on the Lyα origin (e.g. Mas-Ribas et al. 2017). In fact, differently from the several phenomena behind the Lyα emission, the nebular UV continuum radiation is only produced in the ISM around star-forming regions via recombinations of hydrogen ions, while the Balmer lines arise via both recombinations and fluorescence. Therefore, by comparing Balmer lines and UV continuum SB profiles we can determine the importance of nebular against fluorescent emission, while the comparison between Balmer lines and Lyα constrains the impact of scattering phenomena. These studies, however, require deep multiwavelength observations and are hampered by the faintness and small size (both intrinsic and apparent) of distant galaxies.

One possible solution to solve this puzzle is through the study of strongly lensed LAEs (e.g. Swinbank et al. 2007; Karman et al. 2015; Caminha et al. 2016; Patrício et al. 2016; Vanzella et al. 2016, 2020; Smit et al. 2017; Claeyssens et al. 2019, 2022; Chen et al. 2021; Iani et al. 2021). In fact, both lensing effects of magnification and stretching can allow to reach faint fluxes and small scales in short observing time, even though robust lensing models have to be developed in order to correctly interpret and compare the results.

In this context, we study a high-redshift ($z \sim 3.7$) LAE lensed by the Abell 2895 (hereafter A2895; Abell 1958) galaxy cluster ($z \approx 0.227$). Our target (presented in Livermore et al. 2015 as Abell 2895b) has three multiple images (M1, M2, and M3) located at the celestial coordinates (right ascension, declination) of ($1^{\rm h}18^{\rm m}11\overset{\rm s}{.}127$, $-26^\circ57'59\overset{''}{.}36$), ($1^{\rm h}18^{\rm m}10\overset{\rm s}{.}543$, $-26^\circ58'10\overset{''}{.}56$), and ($1^{\rm h}18^{\rm m}10\overset{\rm s}{.}439$, $-26^\circ58'14\overset{''}{.}36$). The multiple images are mirrored with respect to the lensing critical line, i.e. the line of infinite magnification. To investigate the physical properties of our target, we gather a multiwavelength data set that covers its rest-frame UV and optical emission. We study the galaxy rest-frame UV thanks to Very Large Telescope (VLT)/Multi-Unit Spectroscopic Explorer (MUSE) optical integral field spectroscopy with adaptive optics (AO). With VLT/Spectrograph for INtegral Field Observations in the Near-Infrared (SINFONI) AO-assisted NIR integral field spectroscopy we probe the rest-frame optical emission of the target. Thanks to the image multiplicity and the high magnification factor ($\mu = 9 \pm 2$ for the M3 image; Livermore et al. 2015), we are able to probe with unprecedented detail the properties of this source.

This paper is organized as follows. In Section 2, we present the observations in our hand and on which this paper is based. We also briefly discuss the main steps followed for the data reduction. In Section 3, we summarize the technique adopted to obtain the UV and optical spectrum of our target and their analysis. We also describe the procedure to obtain pseudo-narrow-band (NB) images of the main emission lines, as well as the UV continuum. In Section 4, we derive the main properties of our target (e.g. dust extinction, metallicity, and SFR) based on the analysis of the main spectral features derived from its UV and optical spectra. We also analyse in detail the galaxy Lyα emission. In Section 5, we summarize and discuss our findings.

In this paper, we adopt a flat Λ cold dark matter (ΛCDM) cosmology with $\Omega_\Lambda = 0.7$, $\Omega_{\rm m} = 0.3$, and $H_0 = 70\,{\rm km\,s^{-1}\,Mpc^{-1}}$. All the wavelengths presented in the following (also in the ions nomenclature) are in vacuum.

2 OBSERVATIONS AND DATA REDUCTION

In the following, we describe the observations and the steps performed for the data reduction. The properties of the MUSE observations and the description of the lensing model adopted were already presented in Iani et al. (2021). Hence, hereafter we only provide a short description of the MUSE observing programme. We refer the reader to Iani et al. (2021) for further details.

During the analysis of our target, we serendipitously found additional LAEs at $z \simeq 4.57$, 4.65, and 4.92. We report their properties in Appendix A.

2.1 MUSE data

We observed the central region of the A2895 galaxy cluster with VLT/MUSE (Bacon et al. 2010), in Wide Field Mode (WFM, 1×1 arcmin^2 field of view – FoV) and with ground-layer adaptive optics (GLAO) provided by the Ground Atmospheric Layer Adaptive Optics for Spectroscopic Imaging (GALACSI) module (Arsenault et al. 2008; Ströbele et al. 2012). The observations were carried out during the 2017 Science Verification of GALACSI (Leibundgut et al. 2017; Programme ID: 60.A-9195(A), PI: A. Zanella), and in 2019 August (Programme ID: 0102.B-0741(A), PI: A. Zanella), for a total exposure time of 5 h. The MUSE WFM observations cover a wavelength range $\Delta\lambda = 4750$–9350 Å (nominal) with a spectral resolution $R \sim 3000$. We reduce the data following the standard reduction procedure (i.e. corrections for bias, flat-field, wavelength and flux calibration, atmospheric extinction, and astrometric correction) by means of the ESO reduction pipeline[1] (ESOREX), version 2.4.1 (Weilbacher et al. 2012, 2014), and the Zurich Atmosphere Purge (ZAP),[2] version 2.1, software (Soto et al. 2016) to properly account for sky residuals. We reconstruct the MUSE point spread function (PSF) via the publicly available algorithm PSFR[3] (Fusco et al. 2020),

[1] https://www.eso.org/sci/software/cpl/esorex.html
[2] https://zap.readthedocs.io/en/latest/
[3] https://muse-psfr.readthedocs.io/en/latest/

and find a full width at half-maximum (FWHM) of 0.4 arcsec, as requested for the observations.

2.2 SINFONI data

The multiple image M3 of our target was observed with the *K*-band grating ($\Delta\lambda = 1.95$–2.45 μm, $R \sim 4000$) of SINFONI (Eisenhauer et al. 2003; Bonnet et al. 2004), between 2011 August 29 and September 25 (Programme ID: 085.B-0848(A), PI: J. Richard), for a total exposure time of 6 h with AO (natural guide star mode). The image quality of the observations is $\simeq$0.17 arcsec in *K* band, as measured from the standard telluric star observed close in time and airmass to the target, and used for flux calibration. We reduce the data with the ESO SINFONI pipeline (ESOREX, version 3.13.2) following the standard procedure: correction for dark current, bad pixels and distortions, flat-field, and wavelength calibration. We also correct for telluric features, flux calibrate, and stack science exposures within the same observing block (OB). After the reduction of the single OBs, we correct their wavelength calibration for the barycentric velocity, a step that is not automatically performed by the reduction pipeline. We register the astrometry of the final SINFONI data cube to the one of MUSE by minimizing the spatial offset between the centroid of the [O III] λ5008 emission and that of the target UV continuum. We follow this procedure since no other target falls within the SINFONI FoV and the optical continuum of our source is undetected (see Section 3 and bottom panel of Fig. 1). Furthermore, the overlap between UV continuum and optical [O III] λ5008 emission ensures the spatial overlap with more energetic transitions of the same ion, i.e. O III] λλ1660, 1666.

3 ANALYSIS

In the following section, we report the procedures adopted to extract the UV and optical spectrum of our target and the methodology applied to derive the main properties of the spectral features presented in Table 1 (e.g. line fluxes and EWs).

3.1 Extraction of the spectra

Following Iani et al. (2021), we extract the UV and optical spectrum of our target considering the spatial extent of the galaxy brightest UV and optical emission lines, i.e. the Lyα and [O III] λ5008, respectively. As a first step, we create pseudo-NB images that maximize the signal-to-noise ratio (SNR) of these lines (refer to Iani et al. 2021, for more details).

We create maps of SNR that we use to define the areas where to extract the galaxy optical and UV spectrum. The extraction is performed by summing up the spectra corrected for the lensing magnification factor of all the spaxels where the SNR is $\geq$2.5. Since the MUSE data cover all the three multiple images (M1, M2, and M3) of our target, while SINFONI observed only M3, we repeat this procedure separately for each multiple image, after cleaning the MUSE UV spectrum from the optical stellar continuum of the A2895 brightest cluster galaxy (see Iani et al. 2021). Finally, we average the UV spectrum of each multiple image to increase the SNR. In Fig. 1, we present the UV (upper panel) and optical (lower panel) spectra of our target.

3.2 Emission and absorption line measurements

The spectra display several UV and optical emission lines, as well as a few weak UV absorption features. We fit all the lines (but the Lyα) with a Gaussian profile, after modelling their local stellar continuum. We study the Lyα separately because of its resonant nature and asymmetric spectral profile; see Section 4.6.1. To determine the uncertainties on the values derived from the Gaussian fit of each line, we perform 1000 Monte Carlo realizations of the spectra. Each realization is drawn randomly from a Gaussian distribution with mean and variance corresponding to the observed spectrum flux and variance. We define the uncertainty on the line properties as the half-distance between the 16th and 84th percentiles. In Table 1, we present the results of our fit for all the lines with an estimated SNR > 3. As in Iani et al. (2021), we add to the final errors also the flux systematic uncertainties due to absolute flux calibration, equal to 5 per cent and 20 per cent for MUSE[4] and SINFONI data, respectively.

By averaging the wavelength position of the emission lines (but Lyα) we estimate the galaxy systemic redshift $z_{\rm sys} = 3.72096 \pm 0.00012$. For the redshift estimate, we do not consider absorption lines as they are weak spectral features in our UV spectrum and can be blueshifted whenever the galaxy ISM is characterized by outflows (e.g. Pettini et al. 2000; Dessauges-Zavadsky et al. 2010; Patrício et al. 2016).

Finally, we measure the rest-frame equivalent width (EW_0) of each line. We use a definition of EW_0 in which negative values indicate emission, while positive values refer to absorption. Since the optical continuum of the galaxy is not detected in the SINFONI data, we report a 3σ upper limit[5] on the line flux and that corresponds to a 3σ lower limit on the line EW_0.

4 GALAXY PROPERTIES

In the following section, we derive the physical properties (e.g. dust extinction, nebular metallicity, and SFR) of our target.

4.1 Dust extinction

We estimate the dust extinction in a twofold way: by considering the slope of the UV continuum (β-slope) and from the ratio of the Balmer lines Hγ/Hβ (*Balmer decrement*).

For the UV β-slope, we define seven spectral windows in the range 1200–2000 Å (see Table 2) that remove from the fitting procedure all the relevant absorption features of stellar UV spectra, as well as the MUSE Na notch filter, and fit the observed UV continuum of our target with a power law, i.e. $f(\lambda) \propto \lambda^{\beta}$ (e.g. Calzetti, Kinney & Storchi-Bergmann 1994; Castellano et al. 2012). From the fit we obtain $\beta = -2.6 \pm 0.5$. Such low value of the β parameter is typical of stars with steep blue UV slopes, i.e. young and unobscured stellar populations. In fact, if we convert the measured β into the colour excess of the stellar continuum $E(B-V)_{\rm cont}$ via the relation by Meurer, Heckman & Calzetti (1999), we obtain $E(B-V)_{\rm cont} \lesssim 0.03$. Despite the fact that the β–$E(B-V)_{\rm con}$ relation depends on metallicity and star formation history (SFH; e.g. Kong et al. 2004; Reddy et al. 2010, 2018; Schaerer, de Barros & Sklias 2013; Zeimann et al. 2015), as well as on stellar mass and age (e.g. Buat et al. 2012; Zeimann et al. 2015; Bouwens et al. 2016b), these values are in line

[4]We tested the MUSE flux calibration against the *Hubble Space Telescope* (*HST*)/Advanced Camera for Surveys (ACS) F606W observations (the only available *HST* image in A2895, SNAP Program 10881, PI: G. Smith) for a total of 25 sources falling in the MUSE FoV, and found a good agreement (median magnitudes offset $\leq$0.01 mag).

[5]We estimate σ as the median of the error spectrum in the wavelength range within which the line fit is performed.

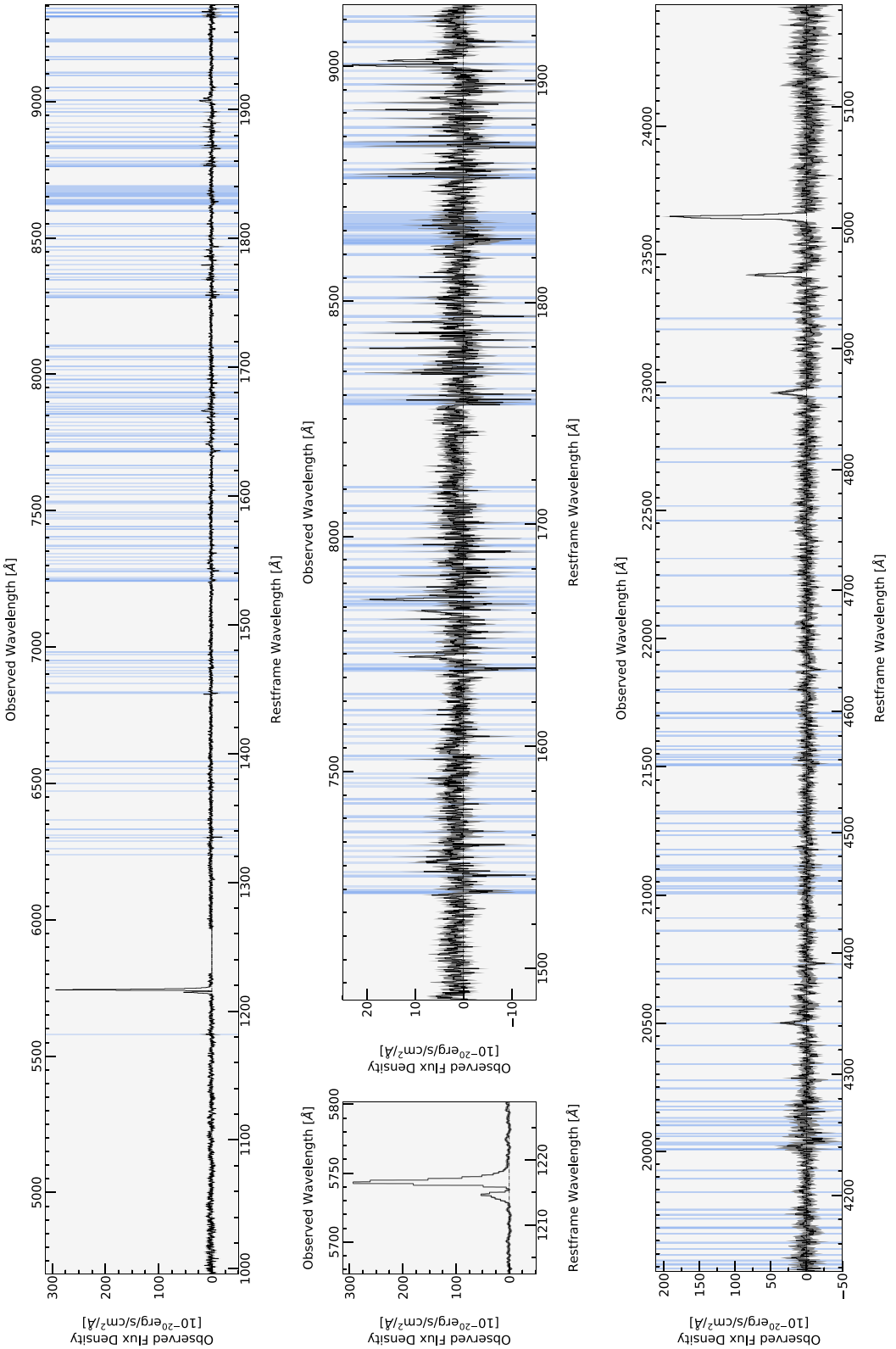

Figure 1. The rest-frame UV (upper panels) and optical spectrum (bottom panel) of our target galaxy. The grey-shaded regions display the $\pm 1\sigma$ error around the spectra, while the vertical light-blue solid lines show the wavelength position of strong telluric lines. In the central panels, we present a zoom-in of the UV spectrum around the Lyα line (left-hand panel) and the UV continuum redwards the Lyα and MUSE notch filter (right-hand panel).

Table 1. Properties of the emission and absorption lines with measured signal-to-noise ratio (SNR) > 3. Unless differently stated, the measurements reported refer to the intrinsic values, i.e. corrected for lensing magnification.

Line	λ_0^a (Å)	Flux^b (10^{-20} erg s^{-1} cm^{-2})	EW$_0^c$ (Å)	z^d	σ^e (km s^{-1})
Ni II	1370.132	-20.2 ± 5.0	1.7 ± 0.4	–	104 ± 45
O V	1371.292	-18.7 ± 4.1	1.6 ± 0.3	–	46 ± 31
Si IV	1393.755	-15.9 ± 3.8	1.4 ± 0.3	–	176 ± 7
Si II	1526.707	-18.4 ± 4.1	2.3 ± 0.5	–	42 ± 41
Si II*	1533.431	8.0 ± 1.7	-1.0 ± 0.2	3.72036 ± 0.00001	6 ± 1
C IV	1548.195	29.7 ± 3.4	-3.9 ± 0.4	3.72072 ± 0.00023	72 ± 22
He II	1640.417	44.5 ± 3.5	-7.8 ± 0.6	3.72087 ± 0.00008	64 ± 13
O III]	1660.809	27.4 ± 4.0	-4.8 ± 0.7	3.72097 ± 0.00019	34 ± 14
O III]	1666.150	79.7 ± 8.4	-12.3 ± 1.3	3.72095 ± 0.00015	51 ± 11
Al II	1670.787	9.2 ± 1.4	-1.4 ± 0.2	3.72041 ± 0.00001	47^{+51}_{-47}
Si III]	1892.029	25.6 ± 1.3	-4.8 ± 0.3	3.72110 ± 0.00002	47 ± 2
[C III]	1906.680	96.6 ± 11.6	-18.1 ± 2.3	3.72095 ± 0.00015	44 ± 17
C III]	1908.734	72.2 ± 12.0	-13.4 ± 2.3	3.72119 ± 0.00039	58 ± 46
Hγ	4341.680	365.8 ± 99.4	$\leq -2.3^\dagger$	3.72151 ± 0.00030	14^{+162}_{-14}
[O III]	4364.436	178.1 ± 63.1	$\leq -1.2^\dagger$	3.72027 ± 0.00084	67 ± 53
Hβ	4862.680	652.9 ± 141.2	$\leq -3.9^\dagger$	3.72160 ± 0.00024	62 ± 28
[O III]	4960.295	988.6 ± 204.9	$\leq -5.5^\dagger$	3.72147 ± 0.00009	21^{+24}_{-21}
[O III]	5008.240	2909.7 ± 584.3	$\leq -15.5^\dagger$	3.72147 ± 0.00004	50 ± 5

[a]The wavelengths reported are in vacuum.
[b]The flux uncertainties have been increased by 5 per cent (MUSE) and 20 per cent (SINFONI) to take into account errors on the absolute calibration of the data sets.
[c]Rest-frame equivalent width (EW) of the line (the † highlights lines for which the EW$_0$ has been estimated taking into account an upper limit on the stellar continuum flux). We follow the convention for which the EW of emission lines is reported with negative values (see Section 3.2).
[d]Estimated redshift of the target according to the wavelength of the best-fitting Gaussian peak (only for nebular emission lines, as absorption lines might have blueshifted spectral profiles due to outflows, see Section 4).
[e]Velocity dispersion σ corrected for instrumental broadening (see Iani et al. 2021) and in units of km s^{-1}.

Table 2. Rest-frame UV spectral windows employed for the measurement of the stellar continuum β-slope, see Section 4.1.

Window number	Wavelength range (Å)
1	1268–1284
2	1360–1371
3	1407–1515
4	1562–1583
5	1677–1725
6	1760–1833
7	1930–1950

with results found for other low-mass galaxies at intermediate/high redshifts (e.g. Bouwens et al. 2010, 2016a; Castellano et al. 2012; Vanzella et al. 2018; Iani et al. 2021).

Thanks to the simultaneous detection of Hγ and Hβ, we can estimate the nebular extinction due to dust from the observed ratio Hγ/Hβ. For our target, we derive $(\mathrm{H}\gamma/\mathrm{H}\beta)_{\rm obs} = 0.56 \pm 0.11$. Adopting the attenuation law by Calzetti et al. (2000) and an intrinsic Balmer decrement of $(\mathrm{H}\gamma/\mathrm{H}\beta)_{\rm int} = 0.476$ (from case B recombination; e.g. Osterbrock 1989),[6] we obtain a nebular colour excess of $E(B-V)_{\rm neb} = 0.34^{+0.41}_{-0.34}$. Despite the tension between the face-value estimates, the wide error bars make the nebular estimate compatible with the one obtained from the β-slope.

In the following we always refer to the observed values of the fluxes without taking into account any dust correction (unless differently specified).

4.2 Electron temperature and density, nebular metallicity, ionization parameter, and (C/O) abundance

Thanks to the presence of the [O III] optical lines at 4364, 4959 and 5008 Å, we evaluate the electron temperature $T_{\rm e}$ of the emitting gas following the empirical equation by Proxauf, Öttl & Kimeswenger (2014). The electron temperature we derive is of $T_{\rm e} = (2.2 \pm 0.2) \times 10^4$ K.

In a similar manner, because of the detection of the [C III] doublet at 1908 Å, we determine the electron density $n_{\rm e}$ from the intensity ratio [C III] λ1907/C III] λ1909. By means of PyNeb and assuming $T_{\rm e} = (2.2 \pm 0.2) \times 10^4$ K, we derive an upper limit on the $n_{\rm e} \lesssim 3 \times 10^4$ cm^{-3}.

The UV emission lines detected in our target spectrum allow us to estimate its nebular metallicity by means of the He2–O3C3 diagnostic diagram by Byler et al. (2020), see Fig. 2. The He2–O3C3 diagram has been found to robustly determine the ISM metallicity of metal-poor (subsolar) systems. Specifically, through equation (8) by Byler et al. (2020), we derive an ISM metallicity $12 + \log_{10}(\mathrm{O/H}) = 7.36 \pm 0.02$. Assuming a solar value of $12 + \log_{10}(\mathrm{O/H})_\odot = 8.69 \pm 0.05$ (Allende Prieto, Lambert & Asplund

[6]Case B recombination assumes that all the ionizing photons are processed by the gas ($f_{\rm esc}^{\rm LyC} = 0$). Variations in both the ISM electronic temperature $T_{\rm e}$ and density $n_{\rm e}$ affect the expected Balmer ratio Hγ/Hβ. The 0.476 ratio between Hγ and Hβ is predicted for $T_{\rm e} = 2 \times 10^4$K, $n_{\rm e} = 10^4$ cm^{-3}, and in the absence of an AGN (Osterbrock 1989).

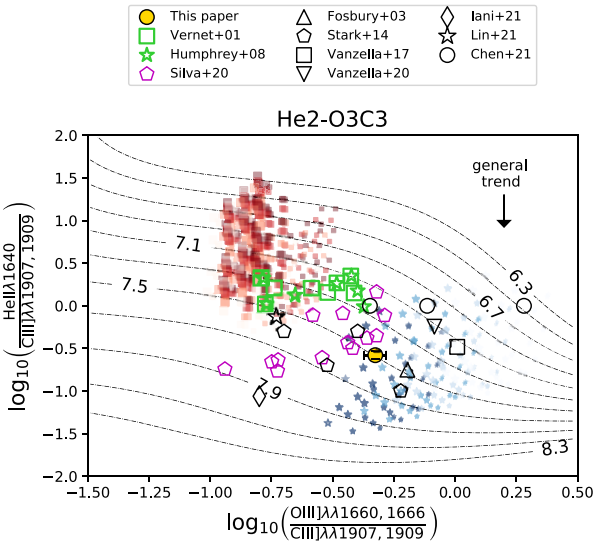

Figure 2. He2–O3C3 diagnostic diagram. The coloured solid lines (from equation 8 in Byler et al. 2020) show how the line ratios vary as a function of the nebular metallicity. The yellow circle displays the position of our target in this diagram, while the open marks are representative points of a sample of intermediate-/high-z sources taken from literature (in black; Fosbury et al. 2003; Stark et al. 2014; Vanzella et al. 2017, 2020; Chen et al. 2021; Iani et al. 2021; Lin et al. 2022), a sample of high-z radio galaxies (in green; Vernet et al. 2001; Humphrey et al. 2008) and a sample of type II quasars (in magenta; Silva et al. 2020). The blue stars show the area of the diagram populated by the stellar models by Gutkin et al. (2016) with subsolar metallicities (more details in Section 4.3.2). The size of these representative points is linked to their ionization parameter U (larger the size, higher the ionization parameter), while their shade of blue depends on the $(C/O)/(C/O)_{\odot}$ (darker the colour, higher the ratio). In a similar way, we present the ratio of nebular emissions for the AGN models by Feltre, Charlot & Gutkin (2016) with red squares. The size of these representative points is still linked to their ionization parameter U, while their shade of red depends on the $(C/O)/(C/O)_{\odot}$ (darker the colour, higher the ratio). Finally, we highlight with a black arrow in the top right-hand side corner the effect of a correction for stellar emission on the He II λ1640 line.

2001), the derived estimate corresponds to a subsolar metallicity of $Z_{\rm neb} = 0.05 \pm 0.02\ Z_{\odot}$, i.e. $Z_{\rm neb} = (7 \pm 3) \times 10^{-4}$.

In their work, Byler et al. (2020) do not provide any relation to determine the ionization parameter (U) as in the case of the nebular metallicity. However, from the comparison with the model grids, we estimate $\log_{10}(U) \sim -2.5$.

We finally investigate the (C/O) abundance of our target by using equations (6) and (7) by Pérez-Montero & Amorín (2017). From the equations, we obtain $\log_{10}(\mathrm{C/O}) = -0.99 \pm 0.23$. If we compare this estimate to the solar value $(C/O)_{\odot} = 0.44$ (Gutkin, Charlot & Bruzual 2016), we derive a ratio $(C/O)/(C/O)_{\odot} \simeq 0.23$. The (C/O) estimate is in agreement with the (C/O)–metallicity relation and with the values found in metal-poor high-ionization dwarf local galaxies and halo stars (e.g. Berg et al. 2016, 2019). Interestingly, because carbon and oxygen are thought to originate primarily from stars of different mass ranges (with O synthesized mostly in massive stars with $M > 10\ M_{\odot}$, while C is produced in both massive and intermediate-mass stars, i.e. $2 < M < 8\ M_{\odot}$), the low (C/O) measured could be interpreted as the consequence of a top-heavy initial mass function (IMF) and/or the sign that we are looking at a very recent burst of star formation. In fact, while in the first case an overabundance of massive stars could bring to an enhanced production of O over C, the same effect could be obtained if the stellar population had just recently formed and only Type II supernovae (SNe) had time to enrich the ISM ($\lesssim$40 Myr; e.g. Veilleux, Cecil & Bland-Hawthorn 2005).

4.3 The source of the ISM ionization: AGN, SF, or shocks?

Different mechanisms (e.g. star formation, AGN, and shocks) can ionize the ISM of galaxies, thus driving the emission of lines in the UV and optical. To discriminate between the different processes, several tracers can be probed, e.g. the width of emission lines, the presence of asymmetries and broadening in their shapes, the detection of specific atomic transitions of heavy elements, and emission line ratios.

4.3.1 Detection, shape, and width of UV metal lines

From the UV and optical spectrum, the emission line profiles do not show the presence of blue/red wings nor broad components. All the emission lines are narrow, having a $\sigma \leq 100$ km s^{-1} (see Table 1) and being unresolved or marginally resolved at the spectral resolution of our data. These results disfavour the hypothesis that our target hosts an unobscured (type I) AGN (e.g. McCarthy 1993; Corbin & Boroson 1996; Humphrey et al. 2008; Matsuoka et al. 2009). This is also supported by the fact that the publicly available X-ray catalogue based on *Chandra* observations (*Chandra* Source Catalog, v. 2.0; Evans et al. 2019, 2020)[7] for this cosmological field does not report any X-ray emitter at our target coordinates nor in its closest vicinity.[8]

However, we cannot fully rule out the possible presence of an obscured (type II) AGN. In fact, the UV spectrum of our target shows several high ionization potential transitions of He and metals, e.g. C IV λ1550 and He II λ1640, whose presence could be explained by AGN activity. This hypothesis could also be supported by the high EW_0 measured for the He II line ($\sim$−8 Å). In fact, recent literature has shown that photoionization models fail to reproduce such rest-frame EW with the only contribution of stars (e.g. Berg et al. 2018; Nanayakkara et al. 2019). A line that is generally considered to be the smoking-gun proof of an AGN is N V λ1240, having an ionization potential of $\sim$78 eV, difficult to explain with the typical emission of stellar populations (e.g. Hainline et al. 2011; Laporte et al. 2017; Grazian et al. 2020). Yet, the MUSE Na notch filter prevents us from detecting this line.

4.3.2 UV spectroscopic diagnostic diagrams

A possible way to better constrain the nature of our target is to consider empirical spectroscopic diagnostic diagrams based on the ratio of UV lines. Similarly to the optical Baldwin–Phillips–Terlevich (BPT) and BPT-like diagrams (Baldwin, Phillips & Terlevich 1981; Veilleux & Osterbrock 1987; Dopita & Sutherland 1995), the ratio between close-by UV emission lines is effective in discriminating among different mechanisms of ISM ionization (e.g. Feltre et al. 2016; Nakajima et al. 2018; Hirschmann et al. 2019). Besides, the

[7]The *Chandra* Source Catalog (CSC) is available at https://cxc.cfa.harvard.edu/csc2/

[8]The *Chandra* observations for this field (ID proposal: 9429, PI: G. P. Smith) were carried out with the imaging mode of the Advanced CCD Imaging Spectrometer (ACIS-I) and have a 3σ depth at the positions of the source of $\simeq 2.3 \times 10^{-15}$ erg s^{-1} cm^{-3}. The *Chandra* images are available at https://cda.harvard.edu/chaser/

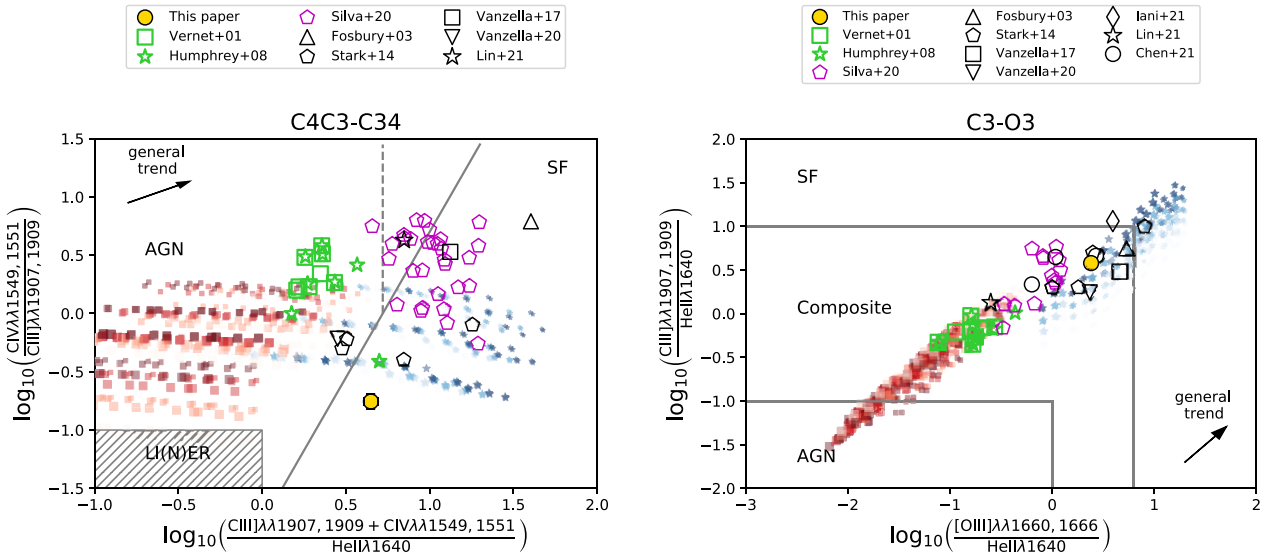

Figure 3. C4C3–C34 (left-hand panel) and C3–O3 (right-hand panel) empirical diagnostic diagrams. The yellow circle displays the position of our target in these diagrams, while the open marks display the position of a sample of intermediate-/high-z sources taken from literature (in black; Fosbury et al. 2003; Stark et al. 2014; Vanzella et al. 2017, 2020; Chen et al. 2021; Iani et al. 2021; Lin et al. 2022), a sample of high-z radio galaxies (in green; Vernet et al. 2001; Humphrey et al. 2008), and a sample of type II quasars (in magenta; Silva et al. 2020). The blue stars show the area of the diagram populated by the stellar models by Gutkin et al. (2016). In a similar way, we present the ratio of nebular emissions for the AGN models by Feltre et al. (2016) with red squares. For both models, the size and colour of the representative points follow the convention presented in Fig. 2. In both panels, the black arrow in the corner highlights the effect of a correction of the He II λ1640 and C IV λ1550 (only in the C4C3–C34 panel) emission. In the C4C3–C34 diagram, the demarcation lines are taken from Nakajima et al. (2018). In the C3–O3 diagram, we resort to the separation lines by Hirschmann et al. (2019).

fact that these diagrams feature the intensity ratio of lines that are close in wavelength makes them rather insensitive to dust extinction.

In our work, we exploit the C4C3–C34, C3–O3, and He2–O3C3 diagrams (e.g. Nakajima et al. 2018; Hirschmann et al. 2019; Byler et al. 2020), see Figs 2 and 3. For the C4C3–C34 diagram, we highlight the demarcation lines between AGN and star-forming galaxies presented in Nakajima et al. (2018). In the case of the C3–O3 diagnostic, we resort to those of Hirschmann et al. (2019). We populate the panels with other metal-poor intermediate-/high-redshift sources taken from the literature (Fosbury et al. 2003; Stark et al. 2014; Vanzella et al. 2017, 2020; Chen et al. 2021; Iani et al. 2021; Lin et al. 2022), a sample of high-z radio galaxies (HzRGs) by Vernet et al. (2001) and Humphrey et al. (2008), a sample of type II quasars from Silva et al. (2020), as well as from theoretical models[9] of both star-forming galaxies (blue stars; Gutkin et al. 2016) and AGNs (red squares; Feltre et al. 2016). We limit both theoretical models to subsolar metallicities $Z = [0.0001, 0.0002, 0.0005, 0.001]$ and ionization parameters $\log_{10}(U) = [-3, -2.5, -2]$. As for the stellar models,[10] we apply an additional cut to $(\mathrm{C/O})/(\mathrm{C/O})_{\odot} = [0.14, 0.20, 0.27, 0.38]$ and an upper cut-off stellar mass for the IMF $M_{\mathrm{up}} = 300\ \mathrm{M}_{\odot}$. The constraints on the ISM metallicity, ionization parameter, and (C/O) abundance are based on the estimates that we retrieved in Section 4.2. On the contrary, we do not limit the stellar and AGN models either in gas density $n_{\mathrm{H}} = [100, 1000]\ \mathrm{cm}^{-3}$ or in dust-to-metal mass ratios $\xi_{\mathrm{d}} = [0.1, 0.3, 0.5]$. Finally, the AGN models[11] have UV spectral slopes α ($f_{\nu} \propto \nu^{\alpha}$) ranging from $[-2, -1.7, -1.4, -1.2]$.

On one hand, according to the demarcation lines by Nakajima et al. (2018) (grey lines in the C4C3–C34 diagram), our target seems to be a star-forming galaxy. On the other hand, based on the redshift-independent separation criteria by Hirschmann et al. (2019), the representative point of our target in the C3–O3 diagram lays at the edge of the *composite* region, i.e. galaxies that are characterized by both ongoing star formation and AGN activity. Depending on the luminosity of the hosted AGN L_{AGN} with respect to star formation ($f = L_{\mathrm{AGN}}/L_{\mathrm{SF}}$), the representative points of sources in the composite region can tend more towards the SF ($f < 0.5$) or AGN ($f > 0.5$) areas. According to the position of our galaxy, the contribution of the AGN luminosity would be less than 0.5 times the one of SF. The composite locus is, however, an area of the diagnostic diagram that is not uniquely determined: theoretical models show that it can also be consistently populated by galaxies whose emission lines originate from shocks (the so-called *shock-dominated* galaxies; e.g. Hirschmann et al. 2019), as well as *pure* SF and AGN models (Feltre et al. 2016; Gutkin et al. 2016). Hence, it is difficult to pinpoint the mechanism that originates the observed UV lines. None the less, by comparing the position of our target with the available theoretical models, we observe a higher compatibility of our estimates with the synthetic stellar models by Gutkin et al. (2016). This is also observed in the He2–O3C3 diagram where we do not have separation lines for the different mechanisms. However, we record a net separation between the AGN and star formation models, with the representative

[9]The models are available at http://www.iap.fr/neogal/models.html

[10]The line fluxes presented in the stellar models by Gutkin et al. (2016) are in units of solar bolometric luminosity (i.e. 3.826×10^{33} erg s^{-1}) per unit SFR (in $\mathrm{M}_{\odot}\ \mathrm{yr}^{-1}$), and assuming a constant SFR with a Chabrier IMF sustained for 10^8 yr.

[11]The line fluxes presented in the AGN models by Feltre et al. (2016) correspond to an accretion luminosity of the central source of 10^{45} erg s^{-1}, and that line luminosities scale linearly with this quantity.

point of our galaxy laying in the area populated by the models by Gutkin et al. (2016).

A word of caution has to be spent, however, in interpreting the results presented in these diagnostics. In fact, the diagrams should be constructed considering the ratio of nebular lines only, i.e. lines emitted by the ionized ISM. However, the intensity of C IV can be affected by stellar absorption, whereas the He II emission can come from both stars and the ionized ISM (Brinchmann, Pettini & Charlot 2008; Erb et al. 2010). This implies that both the C IV and He II observed intensities should be corrected for these effects. The corrections would bring to an enhancement of the C IV flux and a decrease of the He II intensity. In the pure AGN scenario there would be no need of such corrections for He II (see Nakajima et al. 2018, and references therein). The C IV and He II intensity used to construct the diagrams presented here have been directly obtained from the fit of the observed spectrum of our target. We are therefore assuming that the He II flux is only originated by the ionized ISM, while the C IV is not affected by stellar absorption and by the possible presence of a P Cygni profile originated by stellar winds. With the data at our disposal, we cannot apply any realistic flux correction to C IV and He II. Besides, the corrections have been found to depend on several stellar population parameters as metallicity and age, as well as if binary stellar evolution is taken into account (Erb et al. 2010; Steidel et al. 2016). For completeness, however, we report with an arrow the general trend of the above-mentioned corrections in the corner of each panel (the length of the arrow along the two axes is not related to the relative strength of the correction). We highlight how, for all diagrams, the introduction of corrections in the C IV and He II flux would move the representative point of our target even more towards the region of star-forming galaxies. Besides, we observe a net separation between our target and the population of HzRGs from Vernet et al. (2001) and Humphrey et al. (2008), as well as the sample of type II quasars from Silva et al. (2020). This result reinforces the idea that our target is a star-forming galaxy.

4.4 Star formation rate

Assuming that our target is a star-forming galaxy, we estimate its integrated star formation rate (SFR) in a twofold way: from the luminosity of the hydrogen Balmer lines, and from the luminosity of the stellar UV continuum. In both cases, we start from the recipes by Kennicutt (1998) modified for a Chabrier IMF.[12]

For the Balmer lines, the original Kennicutt (1998) prescription is based on the direct conversion of the Hα luminosity into SFR. The estimate that can be derived through this method allows us to probe the so-called *instantaneous* star formation, i.e. the galaxy star formation activity over its last 10 Myr. However, the Hα line is out of the wavelength coverage of our data. To overcome this problem, we convert the Hβ flux into Hα assuming case B recombination (Osterbrock & Ferland 2006).[13] We derive a SFR $=10.7 \pm 2.3\ \mathrm{M_\odot\ yr^{-1}}$.

Similarly, we derive the SFR from the rest-frame UV stellar continuum luminosity. Compared to the Hα–SFR conversion, the UV–SFR relation is based on stronger assumptions, among which a continuous and well-behaved SFH, ongoing typically for at least 100 Myr. Following Kennicutt (1998), we convert the galaxy rest-frame luminosity at 1500 Å, $L_\nu(1500\ \text{Å})$. We extrapolate $L_\nu(1500\ \text{Å})$ from the fit of the UV continuum with a power law, see Section 4.1, and obtain $L_\nu(1500\ \text{Å}) = (7.63 \pm 0.41) \times 10^{27}\ \mathrm{erg\,s^{-1}\,Hz^{-1}}$ and a SFR $= 0.64 \pm 0.03\ \mathrm{M_\odot\ yr^{-1}}$. This estimate, however, does not take into account the correction for the contribution of the nebular UV continuum emission. Although typically weaker at the UV wavelengths than in the optical and NIR, the nebular continuum originates from free–free, free–bound, and *two-photon*[14] transitions, and its contribution to the overall continuum emission depends on several physical parameters among which the ionization parameter U, the temperature of the emitting H II region, the nebular metallicity, and the age of the stellar population emitting the ionizing photons (Byler et al. 2017). By means of PyNeb (Luridiana, Morisset & Shaw 2015) and following Fernández et al. (2018),[15] we estimate a contribution of the nebular continuum to the observed flux at 1500 Å of 50–60 per cent, with the precise estimate depending on the He I/H I and He II/H I abundances. If we assume $T_e = 2 \times 10^4$ K, $n_e = 10^4\ \mathrm{cm^{-3}}$, He I/H I $=$ 0.08, and He II/H I $= 0.02$, we derive $f(1500\ \text{Å})_{\rm neb}/f(1500\ \text{Å})_{\rm obs} =$ 0.53. Hence, correcting the observed UV luminosity at 1500 Å for nebular emission would lower the previous SFR estimate to $0.34 \pm 0.02\ \mathrm{M_\odot\ yr^{-1}}$.

According to our measurements, the SFR(Hα) is about 18 times higher (28 times after correcting for the nebular emission) than the SFR(1500 Å). This significant discrepancy is possibly due to the fact that the assumptions behind the conversion of the two tracers are not fully fulfilled. In particular, the conversion factor in the UV–SFR relation is known to be severely underestimated in the case of a young stellar population ($\lesssim$10 Myr; e.g. Kennicutt 1998; Calzetti 2013). In this regard, the discrepancy between the SFR inferred from the Balmer lines and the UV could favour a *bursty* ongoing star formation against a steady-state process scenario (e.g. Guo et al. 2016; Faisst et al. 2019; Atek et al. 2022). Additionally, deviations on the shape of the IMF and its mass limits, the stellar metallicity and the number of ionizing photons produced can play an important role. To estimate the correction factor that should be taken into account when converting the UV luminosity into SFR in the case of a single burst SFH, we resort to the BPASS models[16] (v. 2.2.1; Eldridge et al. 2017; Stanway & Eldridge 2018). If we assume both a Chabrier and top-heavy IMF[17] with an upper cut-off mass of 300 $\mathrm{M_\odot}$ and a subsolar metallicity ($10^{-5} \leq Z \leq 10^{-3}$), we obtain a correction factor to the L(UV)–SFR relation by Kennicutt (1998) of about 8 at 2–3 Myr, see

[12] To transform from a Salpeter to a Chabrier IMF, we divide by a 1.7 factor.

[13] According to case B recombination the intrinsic ratio Hα/Hβ is equal to 2.74 for a $T_e = 2 \times 10^4$ K and $n_e = 10^4\ \mathrm{cm^{-3}}$.

[14] The two-photon continuum is a bound–bound process where the excited 2s state of hydrogen decays to the 1s state via the simultaneous emission of two photons. The energy of the two photons produces a bump in the UV spectrum at $\approx$1500 Å (Byler et al. 2017).

[15] To estimate the monochromatic flux of the nebular continuum, we apply equation (15) in Fernández et al. (2018):

$$F_{\rm neb} \simeq \frac{\gamma}{\alpha^{\rm eff}_{\rm H\beta}\, h\nu_{\rm H\beta}}\, F(\mathrm{H}\beta),$$

where γ is the nebular continuum emissivity (in erg cm^{-3} s^{-1} Å^{-1}) as estimated from PyNeb (Luridiana et al. 2015) assuming $T_e = 2.2 \times 10^4$ K and $n_e = 3 \times 10^4\ \mathrm{cm^{-3}}$ (see Section 4.2), $\alpha^{\rm eff}_{\rm H\beta}$ is the Hβ effective recombination coefficient ($1.61 \times 10^{-14}\ \mathrm{cm^3\ s^{-1}}$; Osterbrock 1989, p. 84), $h\nu_{\rm H\beta}$ is the energy associated with the Hβ transition (i.e. 4.08×10^{-12} erg), and F(Hβ) is the measured Hβ flux (in erg s^{-1} cm^{-2}).

[16] https://bpass.auckland.ac.nz/9.html

[17] The available BPASS top-heavy IMF is given by

$$N(M < M_{\rm max}) \propto \int_{0.1}^{M_1} \left(\frac{M}{\mathrm{M_\odot}}\right)^{\alpha_1} \mathrm{d}M + M_1^{\alpha_1} \int_{M_1}^{M_2} \left(\frac{M}{\mathrm{M_\odot}}\right)^{\alpha_2} \mathrm{d}M,$$

where $M_1 = 0.5\,\mathrm{M_\odot}$, $M_2 = 300\,\mathrm{M_\odot}$, $\alpha_1 = -1.3$, and $\alpha_2 = -2.0$. For more details on the BPASS IMFs, we refer the reader to the BPASS user manual.

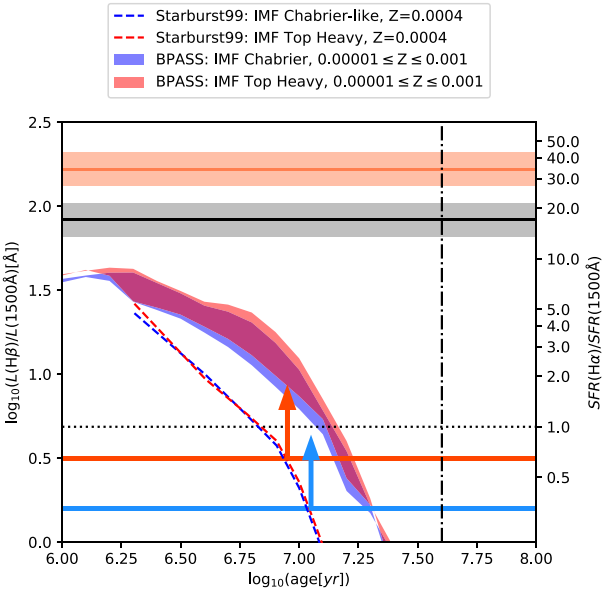

Figure 4. Age versus $L(\mathrm{H}\beta)/L(\mathrm{UV})$ (left) and SFR(Hα)/SFR(1500 Å) (right) ratios diagram. With dashed lines we present the theoretical tracks from STARBURST99 for a Chabrier-like (blue) and top-heavy (red) IMFs. Following the same colour coding, the blue and red shaded areas depict the models from BPASS v. 2.2.1. The horizontal black line shows the observed $L(\mathrm{H}\beta)/L(\mathrm{UV})$ and SFR(Hα)/SFR(1500 Å) ratios for our target and the grey shaded region is representative of its associated error. Similarly, in orange, we show the range of values obtained if we correct the observed ratios for nebular continuum emission. The coloured arrows highlight the ratios lower limits of the aforementioned estimates in the case of dust extinction correction (assuming the upper limit value $E(B-V)=0.75$) with the attenuation curve by Calzetti et al. (2000). The horizontal dotted black line is representative of SFR(Hα)/SFR(1500 Å) = 1. Finally, with a vertical black dash–dotted line we report the upper limit on the age of the galaxy youngest stellar population (40 Myr) if we consider the results from the analysis of the (C/O) abundance, see Section 4.2.

Fig. 4. The magnitude of the correction decreases rapidly with time and shrinks down to a factor of about 2 at 10 Myr. In particular, the BPASS tracks show that both more top-heavy IMFs and lower stellar metallicities increase the magnitude of the correction factor. A similar result is also recovered if we consider spectrophotmetric synthetic models derived via the STARBURST99[18] code (Leitherer et al. 1999). In the case of STARBURST99, we construct the models taking into account a single-burst SFH, a Chabrier-like and top-heavy IMF,[19] the Padova stellar tracks, and a subsolar metallicity $Z = 4 \times 10^{-4}$. For the STARBURST99 tracks, the correction factor is smaller, ∼4 at 2–3 Myr (in agreement with the estimates reported by Santini et al. 2014), if compared to BPASS. This result clearly highlights the impact that the introduction of binary stellar systems (as in BPASS) has in the modelling of the properties of stellar populations in galaxies (see also Reddy et al. 2022).

Despite significant, an increase of a factor of 8 in the estimate of the SFR(1500 Å) is not able to explain alone the discrepancy between our two SFR estimates. The additional introduction of dust extinction could alleviate the tension, see Fig. 4.

[18] https://www.stsci.edu/science/starburst99/docs/parameters.html

[19] For the Chabrier-like IMF, we assume an exponent of −1.3 between 0.01 and 0.5 $\mathrm{M}_\odot$, and −2.3 for stellar masses in the interval 0.5–300 $\mathrm{M}_\odot$. For the top-heavy IMF, we adopt −1.35 between 0.01 and 300 $\mathrm{M}_\odot$ (e.g. Zanella et al. 2015).

4.5 Galaxy mass and stellar population age

The absence of stellar continuum detection in SINFONI and of additional rest-frame optical and NIR data prevent us from deriving a robust estimate of the stellar mass $M_\star$ for our target. However, despite being an indirect and uncertain method, we can infer an upper limit on $M_\star$ based on the mass–excitation (MEx) diagram (Juneau et al. 2011). In fact, assuming that our galaxy is star forming, the ratio between the optical [O III] doublet and Hβ implies a maximum stellar mass on the order of $10^{9.5}$ $\mathrm{M}_\odot$. This puts our target in the typical mass range of LAEs (Ouchi et al. 2020; Pucha et al. 2022) and lensed galaxies at similar redshifts (e.g. Bouwens et al. 2022; Meštrić et al. 2022). Besides, this estimate agrees with the fact that low stellar mass galaxies tend to display larger SFR(Hα)/SFR(UV) ratios (Faisst et al. 2019; Atek et al. 2022).

We estimate the light-weighted age of the stellar population through the ratio between the Hβ and UV continuum luminosity. This ratio is predicted to decrease with increasing stellar age. We derive theoretical tracks from both STARBURST99 and BPASS. For our target, the ratio between the observed luminosities is equal to $\log_{10}(L(\mathrm{H}\beta)/L_\nu(1500\,\text{Å})) = 1.92 \pm 0.10$, see Fig. 4. If we account for the contribution of the nebular continuum, the estimate raises to 2.22 ± 0.10. In both cases, the retrieved values are above the STARBURST99 and BPASS theoretical predictions. Only if we correct for reddening, our results become compatible with the tracks. Assuming the extreme value of $E(B-V) = 0.75$ (i.e. the upper limit derived from the Balmer decrement Hγ/Hβ, see Section 4.1), we obtain stellar ages $\lesssim$10–20 Myr.

4.6 The Lyα emission

In the following section, we present a detailed description of the spectral and spatial properties of the Lyα emission detected in our target.

4.6.1 Spectral properties of the Lyα

The spectral shape of the Lyα emission of our target is double peaked. We model each peak through the asymmetric Gaussian profile introduced by Shibuya et al. (2014b). From the best-fitting model, we obtain a Lyα observed total flux of $(1.66 \pm 0.03) \times 10^{-17}$ erg s^{-1} cm^{-2}, corresponding to a total luminosity of $(2.14 \pm 0.02) \times 10^{42}$ erg s^{-1}. The flux ratio between the blue and red peak is of ∼14 per cent. Since we do not detect any stellar continuum underneath the Lyα, we estimate a Lyα EW$_0$ ≤ -108 Å. This value is obtained by dividing the Lyα flux by the median value of the 1σ error in the spectral region covered by the Lyα line. The estimate is in agreement with the EW$_0$ of other LAEs at similar redshifts and luminosities (e.g. Runnholm, Gronke & Hayes 2021). Despite the smooth spectral profile, we highlight that contributions from He II λ1215 and the O V] $\lambda\lambda$1214, 1218 doublet could partially affect the Lyα estimated flux, luminosity, and EW$_0$. Theoretical models show that the contribution of the He II and O V] doublet varies as a function of several physical parameters: the power-law index of the ionizing radiation, the nebular metallicity Z_{neb}, the ionization parameter U, and the presence and strength of H I absorptions (Humphrey 2019). According to these models and based on our target estimated nebular metallicity and ionization parameter, the He II and O V] lines could contribute from 0.4 (optically thick models) to 8 per cent (optically thin models) to the total Lyα flux. For our object, in the case of an optically thin model, the contaminating flux would be mostly associated with the O V] doublet since

the He II λ1215 flux is negligible ($F(\mathrm{He\,II}\,\lambda1215) = (0.28\text{–}0.33) \times F(\mathrm{He\,II}\,\lambda1640) \simeq 6.8 \times 10^{-20}$ erg s^{-1} cm^{-2}, i.e. 0.4 per cent of the Lyα flux). However, since we do not have direct evidence of the O V] doublet in our spectrum and we cannot more robustly constrain its possible flux from the analysis of other lines (e.g. from N V λ1240 or [Ne V] λ1575; Humphrey 2019), in the following we do not consider corrections to the reported Lyα flux, luminosity, and EW_0.

The separation between the blue and red peak of the Lyα emission is $\Delta v_{\mathrm{peak}} = 459 \pm 38$ km s^{-1}, with the red peak offset from the systemic velocity of 320 ± 36 km s^{-1}. Following the results by Kakiichi & Gronke (2021), the estimated peak separation suggests a Lyman continuum escape fraction $f_{\mathrm{esc}}^{\mathrm{LyC}} \lesssim 15$ per cent. This is also confirmed by the trend recently reported by Schaerer et al. (2022) between the $f_{\mathrm{esc}}^{\mathrm{LyC}}$ and the C43 ratio (i.e. C IV λ1550/C III λλ1906, 1909). According to their study, Schaerer et al. (2022) report that galaxies with C43 < 0.75 typically have Lyman continuum escape fraction below 10 per cent. For our target, the observed C43 ratio is equal to 0.18 ± 0.03, thus reinforcing the conclusion that our target is a weak Lyman continuum leaker.

For case B recombination and no dust extinction, the expected ratio Lyα/Hβ = 31.9.[20] We estimate Lyα/Hβ = 2.4 ± 0.5, a factor of about 13 lower than the theoretical ratio, and that translates into a Lyα escape fraction $f_{\mathrm{esc}}^{\mathrm{Ly}\alpha}$ (i.e. $L_{\mathrm{Ly}\alpha}^{\mathrm{obs}}/L_{\mathrm{Ly}\alpha}^{\mathrm{int}}$) of about 8 per cent. This result is in good agreement with the global Lyα escape fraction typically observed at $z \sim 3$–4 (e.g. Hayes et al. 2011). Besides, this estimate appears to be consistent with other objects with similar EW_0 (e.g. Erb et al. 2016) and with the $f_{\mathrm{esc}}^{\mathrm{Ly}\alpha}$–$\mathrm{EW}_0$ correlation after having properly taken into account the impact of the target's ionizing efficiency ξ_{ion} ($\xi_{\mathrm{ion}} = 1.3 \times 10^{25} \times$ SFR(Hα)/SFR(UV) Hz erg^{-1}; see Sobral & Matthee 2019, and their equation 6, for further details). Interestingly, if we hypothesize that the tension between the theoretical and the observed Lyα/Hβ ratios is only due to dust extinction, we would estimate a colour excess $E(B-V)_{\mathrm{Ly}\alpha} = 0.38 \pm 0.03$ (adopting the attenuation curve by Calzetti et al. 2000) quite in agreement with the nebular colour excess $E(B-V)_{\mathrm{neb}}$ that we estimated from the Hγ/Hβ ratio ($0.34^{+0.41}_{-0.34}$, see Section 4.1).

We apply radiative transfer modelling to the Lyα emission to infer the ISM metal and dust content (e.g. Charlot & Fall 1993), H I and H II regions relative geometries, and the kinematics of the neutral gas (e.g. Verhamme, Schaerer & Maselli 2006; Laursen & Sommer-Larsen 2007) directly from the profile of the Lyα line. We apply an updated version of the pipeline introduced by Gronke, Bull & Dijkstra (2015), implementing 12 960 radiative transfer models derived by means of the code TLAC (Gronke & Dijkstra 2014). The radiative transfer models we adopt are 'shell-models' (e.g. Ahn & Lee 2002; Verhamme et al. 2006), i.e. they consist of a single point-like source emitting Lyα and continuum radiation and surrounded by a shell of neutral hydrogen and dust. Because of their simple geometry, only four parameters are needed to fully describe these models: the shells neutral hydrogen column density $N_{\mathrm{H\,I}}$, their expansion velocity v_{exp} (assuming positive values for outflows, negative in the case of inflows), an (effective) temperature T that includes the effects of small-scale turbulence, and the dust optical depth τ_{d} to parametrize the dust content. Finally, the emitted Lyα is assumed to have an intrinsic Gaussian emission characterized by an intrinsic Lyα equivalent width $\mathrm{EW}_{\mathrm{int}}$, and its width σ_{int}. We carry out the fitting in wavelength space with a Gaussian prior on the redshift z and after degrading the synthetic spectrum to the MUSE spectral resolution at the observed Lyα wavelength (derived from equation 8 in Bacon et al. 2017). According to the best-fitting model, for the shell we obtain $\log_{10}(N_{\mathrm{H\,I}}[\mathrm{cm}^{-2}]) = 16.8 \pm 0.2$, $v_{\mathrm{exp}} = 99 \pm 5$ km s^{-1}, $\log_{10}(T[\mathrm{K}]) = 5.3 \pm 0.2$, and $\tau_{\mathrm{d}} = 0.6 \pm 0.2$, while the Lyα intrinsic emission has $\mathrm{EW}_{\mathrm{int}} = -415 \pm 12$ Å and $\sigma_{\mathrm{int}} = 210 \pm 4$ km s^{-1}. As already pointed out in recent literature (e.g. Orlitová et al. 2018), the intrinsic width of Lyα recovered by the radiative transfer models results to be significantly larger than the one of the Balmer lines (for our target a factor of ∼3.4 larger if compared to our estimate of the Hβ line, in line with the results from Orlitová et al. 2018). According to Li & Gronke (2022), however, this discrepancy is most likely due to additional radiative transfer effects and, in particular, the possibility that the Lyα propagates within a clumpy gas distribution with velocity dispersions $\gtrsim$100 km s^{-1}.

Table 3. The results from the line-fitting procedure and TLAC radiative transfer modelling of the target Lyα emission, see Section 4.6.1. The line flux F(Lyα) and luminosity L(Lyα) are corrected for magnification but not for dust extinction.

Parameter	Value
F(Lyα) (erg s^{-1} cm^{-2})	$(1.66 \pm 0.03) \times 10^{-17}$
L(Lyα) (erg s^{-1})	$(2.14 \pm 0.02) \times 10^{42}$
$F_{\mathrm{blue,\,peak}}/F_{\mathrm{red,\,peak}}$	∼14 per cent
EW_0 (Å)	≤ -108
Δv_{tot} (km s^{-1})	459 ± 38
$\Delta v_{\mathrm{red,\,peak}}$ (km s^{-1})	320 ± 36
$f_{\mathrm{esc}}^{\mathrm{Ly}\alpha}$	0.08 ± 0.02
$f_{\mathrm{esc}}^{\mathrm{LyC}}$	<15 per cent
$\log_{10}(N_{\mathrm{H\,I}})$ (cm^{-2})	16.8 ± 0.2
v_{exp} (km s^{-1})	99 ± 5
$\log_{10}(T)$ (K)	5.3 ± 0.2
τ_{d}	0.6 ± 0.2
$\mathrm{EW}_{\mathrm{int}}$ (Å)	-415 ± 12
σ_{int} (km s^{-1})	210 ± 4

Since 'shell-models' are an oversimplification of the complex structure and kinematics of LAEs and their surroundings, it is currently debated how much of the radiative transfer is indeed captured by the models and the real meaning and reliability of the involved parameters, especially T and τ_{d}. At the same time, it has been shown that the outflow velocity v_{exp} and column density of the 'shell-model' $N_{\mathrm{H\,I}}$ correlate well with the ones of a more realistic multiphase medium (Gronke & Dijkstra 2016), thus making the estimate of these two parameters particularly robust. We report the results obtained from the analysis of the Lyα spectral properties in Table 3.

Finally, we investigate the presence of spatial variations and kinematics patterns in the Lyα spectral shape (e.g. Patrício et al. 2016; Smit et al. 2017; Erb, Steidel & Chen 2018; Claeyssens et al. 2019; Leclercq et al. 2020). To this aim, we extract the 1st moment map of the Lyα spectral distribution and the 0th moment maps created by collapsing the MUSE data cube in velocity bins around the Lyα line. From both methods, we find no coherent kinematic pattern. To increase the SNR of the profiles, we decide to compare the integrated Lyα spectrum extracted within a circular aperture (0.4 arcsec radius) centred at the peak position of the Lyα emission with the Lyα profile observed in the outskirts (circular annulus 0.4–0.8 arcsec). Also in this case, we do not find any difference in the Lyα profile shape of the two regions and in contrast with results from recent studies of other lensed LAEs (e.g. Claeyssens et al. 2019; Chen et al. 2021).

[20] The reported value has been obtained with PyNeb assuming $T_{\mathrm{e}} = 2 \times 10^4$ K and $n_{\mathrm{e}} = 10^4$ cm^{-3}.

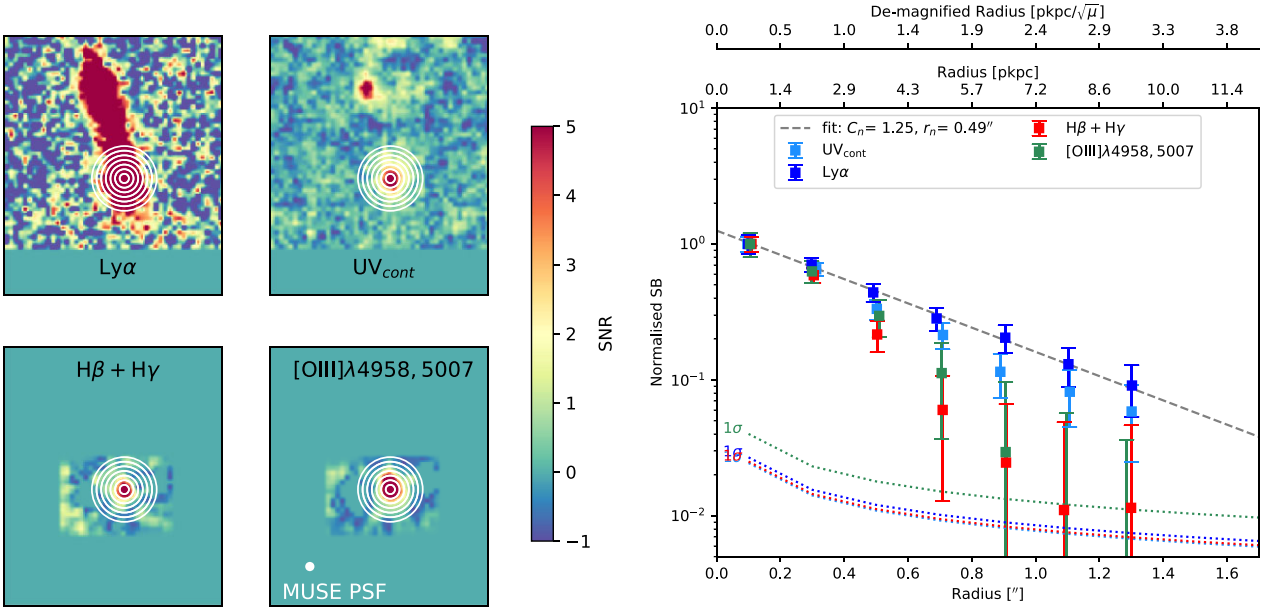

Figure 5. Left-hand panels: SNR maps of the Lyα, UV continuum, Balmer lines, and optical [O III] doublet of our target. The concentric white squares show the areas within which the SB profile of the different tracers (bottom panels) has been extracted. In the left-hand bottom corner of the left-hand side panel, we also report with a white circle the size of the MUSE PSF. Right-hand panel: radial SB profiles of the Lyα, UV continuum, and strongest optical emission lines of our target. The measurements (coloured squares) are normalized to their peak value. The grey dashed line shows the best-fitting exponential profile to the Lyα data points (blue squares), while the coloured dotted lines show the 1σ limit for each tracer.

4.6.2 Spatial extent of the Lyα

Following the procedure described in Section 3.1, we extract the pseudo-NB images of the strongest emission lines of our target, see top panels in Fig. 5. We also create a pseudo-NB image of the galaxy UV continuum emission by collapsing the MUSE data cube in the wavelength windows within which we measured the UV β-slope, see Table 2 and Section 4.1, and stacking them together. Similarly, to increase the SNR of the emission line images we stack the intensity maps of the doublets of the optical [O III]. We also stack together the maps of the two Balmer transitions available, i.e. Hβ and Hγ. Because of the different spatial resolution of the MUSE and SINFONI data, we degrade the resolution of the SINFONI pseudo-NB images to match the one of MUSE. To do so, we first convolve the SINFONI images with a Gaussian kernel to match the MUSE PSF, and then we resample them to the MUSE standard spatial sampling, i.e. 0.2 × 0.2 arcsec^2.

Several statistical studies have shown the existence of an offset between the centroid of the Lyα and UV continuum emission $\delta_{\rm Ly\alpha}$ (e.g. Bunker, Moustakas & Davis 2000; Fynbo, Møller & Thomsen 2001; Shibuya et al. 2014a; Hoag et al. 2019; Ribeiro et al. 2020; Claeyssens et al. 2022). Theoretical studies based on the 3D modelling of Lyα radiative transfer in disc galaxies (e.g. Laursen & Sommer-Larsen 2007; Verhamme et al. 2012; Zheng & Wallace 2014) ascribe the Lyα UV offset to the easier escape and propagation of Lyα photons perpendicularly to the galaxy disc. In this case, the presence of an offset could be explained as a consequence of the viewing angle under which the observer sees the target. Interestingly, Claeyssens et al. (2022) report how the presence of an offset between the galaxy UV emission and the Lyα could also be linked to the mechanism originating the Lyα emission. In the case of small offsets (whenever the Lyα centroid is within the effective radius of the UV emission), Claeyssens et al. (2022) suggest that the offset likely originates from substructures detectable in the UV, such as an off-centre star-forming clump. In the case of larger offsets, other mechanisms could be invoked: gas inflows, scattering effects of the Lyα photons in the CGM, extinction, fluorescence, and emission from faint satellites. To investigate this, we resort to the GALFIT software (Peng et al. 2010). We model the multiple images M2 and M3 of our target simultaneously in both the Lyα and UV continuum map. For each multiple image, we use a single Sérsic profile and obtain smooth residual maps (normalized residuals <20 per cent). From the GALFIT best fit, we estimate an offset between the centroids of the Lyα and UV continuum $\delta_{\rm Ly\alpha} = 0.18 \pm 0.02$ arcsec that corresponds to 1.30 ± 0.17 pkpc. If we correct for magnification,[21] the intrinsic offset results in 0.43 ± 0.07 pkpc. This estimate is in very good agreement with the recent results presented by Claeyssens et al. (2022) who found a median value for the separation of the Lyα and UV continuum centroids of $\delta_{\rm Ly\alpha} = 0.58 \pm 0.14$ pkpc in the analysis of 603 lensed LAEs in the redshift interval $2.9 < z < 6.7$. In addition, our estimate is also in line with the findings by Hoag et al. (2019) and Ribeiro et al. (2020) for LAEs at similar redshifts. Besides, the low $\delta_{\rm Ly\alpha}$ value is in trend with the observed Lyα EW$_0$–$\delta_{\rm Ly\alpha}$ anticorrelation (e.g. Shibuya et al. 2014b; Hoag et al. 2019). Hence, following Claeyssens et al. (2022), the observed offset in our target could be the consequence of an off-centre star-forming clump harboured in our target.

Additionally, we investigate the SB profiles of UV lines and continuum. From each pseudo-NB image, we extract the radial SB profile within concentric apertures centred at the peak of the UV continuum emission and with increasing radii (in steps of 0.2 arcsec) from 0.2 out to 1.4 arcsec (Fig. 5). The UV and optical lines and the UV continuum appear to be all spatially resolved, having a larger

[21] To correct for magnification, we divide the estimated $\delta_{\rm Ly\alpha}$ value for the square root of the magnification factor $\mu = 9 \pm 2$ (see table 2 in Livermore et al. 2015).

spatial extent than the MUSE PSF. In particular, the Lyα and UV continuum are the most spatially extended. By fitting the Lyα SB with an exponential function, i.e. $\mathrm{SB}(r) = C_\mathrm{n} \exp(-r/r_\mathrm{n})$, we obtain a scale length r_n for the Lyα nebula of $r_\mathrm{n}(\mathrm{Ly}\alpha) = (0.49 \pm 0.01)$ arcsec. If we convert into physical kpc and correct for magnification, we infer $r_\mathrm{n}(\mathrm{Ly}\alpha) \simeq 1.2$ pkpc (not corrected for PSF). This value is in good agreement with the typical scale length estimates for Lyα haloes and with the r_n–L(Lyα) correlation (e.g. fig. 13 in Ouchi et al. 2020, and references therein). If we apply the exponential model to the UV continuum and Balmer lines, we derive $r_\mathrm{n}(\mathrm{UV}) = (0.38 \pm 0.02)$ arcsec $\simeq 1$ pkpc and $r_\mathrm{n}(\mathrm{H}) = (0.25 \pm 0.02)$ arcsec $\simeq 0.65$ pkpc. According to the r_n values and the trend of the SB profiles presented in Fig. 5, the Lyα and UV continuum extend more than the Balmer lines.

5 SUMMARY AND DISCUSSION

The multiwavelength analysis of our target highlights that A2895b is a lensed LAE at $z \simeq 3.721$ with a compact UV morphology ($r_\mathrm{n} \simeq 1.2$ pkpc) and a Lyα luminosity of $\simeq 2 \times 10^{42}$ erg s^{-1}. In particular, A2895b is a star-forming galaxy with a SFR estimated from the conversion of the Hβ luminosity of 10.7 ± 2.3 M$_\odot$ yr^{-1}. The MEx diagram (Juneau et al. 2011) suggests that our target has a stellar mass smaller than $10^{9.5}$ M$_\odot$. If we consider the upper limit on the stellar mass and the above SFR, A2895b populates a region of the $M_\star$–SFR plane above the main sequence of star-forming galaxies at $2.8 < z < 4$ (Rinaldi et al. 2022), with a lower limit on its specific SFR of about 3.5×10^{-9} yr^{-1}. This suggests that our target is likely to be a starbursting system.

From the analysis of the nebular UV line ratios, their shape and width, and the absence of an X-ray counterpart (see Section 4.3), we exclude the presence of an AGN. In this regard, the diagnostic diagrams based on UV line ratios clearly show a net separation between the typical values observed in high-z radio galaxies (e.g. Vernet et al. 2001; Humphrey et al. 2008) and type II quasars (Silva et al. 2020), as well as from theoretical predictions of AGNs narrow-line regions (Feltre et al. 2016). This result is also in line with the fact that LAEs hosting AGNs are typically characterized by a Lyα luminosity $L(\mathrm{Ly}\alpha) \gtrsim 2.5 \times 10^{43}$ erg s^{-1}, i.e. one order of magnitude above our estimate (e.g. Konno et al. 2016).

Based on these findings, *in situ* star formation results to be a good candidate for explaining the Lyα emission of our target, whereas we disfavour AGN activity. We also exclude scenarios of both shock heating due to outflows and gravitational cooling. In fact, these processes not only are typically expected to contribute to the Lyα emission at $\gtrsim$20 pkpc from the galaxy centre (e.g. Mas-Ribas et al. 2017, and references therein), but also to significantly increase the number of collisional excitations of the hydrogen atoms, thus bringing to an increase in the measured Lyα/Hβ ratio with respect to what predicted by case B recombination (*super case B objects*; e.g. Otí-Floranes et al. 2012; Nakajima et al. 2013). Specifically, in the case of a significant contribution to the Lyα emission from inflowing gas accreted onto the central galaxy (i.e. gravitational cooling; e.g. Haiman, Spaans & Quataert 2000; Kereš et al. 2005; Dekel & Birnboim 2006; Shull et al. 2009), the Lyα/Hβ ratio is expected to exceed the case B value of more than a factor of 10 (e.g. Dijkstra 2014). None the less, for our target we estimate a Lyα/Hβ ratio 13 times smaller than the case B value, i.e. 1–2 orders of magnitudes below the predictions for shock heating and gravitational cooling (see Section 4.6.1). Besides, for the gravitational cooling hypothesis, signatures of Lyα cooling radiation should be found by the analysis of the Lyα EW. In fact, in this case the Lyα intrinsic EW is expected to exceed the maximum predictions for 'regular' star formation activity (i.e. 300–400 Å in modulus; e.g. Kashikawa et al. 2012). Also in this regard, we do not need to resort to gravitational cooling to explain our measurements ($\mathrm{EW_{int}} = -415 \pm 12$ Å). We highlight, however, that the details of the Lyα emission via gravitational cooling are still debated and remain uncertain (Yang et al. 2006; Dijkstra & Loeb 2009; Faucher-Giguère et al. 2010; Cantalupo, Lilly & Haehnelt 2012; Lake et al. 2015). Ultimately, we discard the hypothesis of fluorescence due to *ex situ* star formation activity (e.g. from satellite sources), or background sources (quasi-stellar objects – QSOs), since we do not find evidence of spectral features of these additional systems in our UV and optical spectra.

The analysis of the spatial extent of the UV continuum, Lyα, and Balmer lines (see Section 4.6.2) arises some interesting points. For our target, the UV continuum and Lyα emissions are more extended than the optical hydrogen transitions Hβ+Hγ. While a more extended Lyα SB profile with respect to the Balmer lines could be the consequence of resonant scattering, the fact that the UV continuum is more extended than the Balmer lines is more puzzling and seems to further provide evidence against fluorescence. In fact, while nebular UV continuum emission follows recombination processes in the ISM, Balmer lines arise from both recombination and fluorescence. Hence, we would expect the nebular UV continuum emission to be more compact than the Balmer lines. A possible way to explain this finding is to consider that the extended UV emission observed originates from an unobscured stellar population with age 20–100 Myr. The existence of such stellar population seems to be supported by the very blue β-slope of our target ($\beta = -2.6 \pm 0.5$, see Section 4.1). If so, A2895b would be hosting (at least) two stellar populations: a newly born population of stars ($\leq$10 Myr) traced by the Balmer lines, and a more extended, 'older' and unobscured stellar population. In this case, the extended Lyα emission could arise from resonant scattering of the Lyα photons produced in the star-forming regions. Interestingly, the presence of two populations could also alleviate the discrepancy of the face value between the dust colour extinction estimated from the UV continuum and Balmer decrement (e.g. *dust-selective extinction*; Calzetti et al. 1994), along with the partial remaining tension between the ratio L(Hβ)/L(UV) and the theoretical stellar models from BPASS and STARBURST99 calculated in the case of top-heavy IMF and subsolar metallicities, see Section 4.5. To verify this hypothesis, deeper observations targeting the galaxy rest-frame optical and IR emission are needed. Such follow-up could also explain the small Lyα offset ($\delta_{\mathrm{Ly}\alpha} \simeq 0.6$ pkpc) detected with respect to the UV continuum and Balmer lines. In fact, if $\delta_{\mathrm{Ly}\alpha}$ is a consequence of an off-centre star-forming clump (e.g. Claeyssens et al. 2022), we would expect the Lyα peak to be coincident with the peak of the Balmer lines. However, this discrepancy could be a mere effect of how the astrometry of the SINFONI data set has been registered to MUSE. As explained in Section 2.2, we registered the SINFONI astrometry to the MUSE one by minimizing the spatial offset between the centroid of the optical [O III] emission and the target UV continuum. By doing so, we also overlapped the centre of the optical and UV [O III] emissions. We followed this procedure since no other target falls within the SINFONI FoV and the optical continuum of our source is undetected. In this sense, rest-frame optical observations with a more robust astrometry could shed light on this aspect.

6 CONCLUSIONS

In this paper, we presented a detailed study of the integrated UV and optical properties of A2895b, a lensed LAE at $z \simeq 3.721$ in the

background of the A2895 galaxy cluster. The analysis was based on the AO-assisted integral field spectroscopy of MUSE and SINFONI. From our study, we inferred the following.

(i) Our target has a steep blue UV continuum ($\beta = -2.6 \pm 0.5$). Such blue continuum is possibly the sign of a young, unobscured stellar population.

(ii) The analysis of the shape of spectral lines along with empirical diagnostic diagrams based on UV line ratios (C4C3–C34, C3–O3, and He2–O3C3) suggests that our target is a star-forming galaxy with a current SFR $= 10.7 \pm 2.3$ $M_\odot$ yr^{-1} (from the Hβ line luminosity; Kennicutt 1998). We exclude the presence of an AGN harboured in the galaxy centre.

(iii) The galaxy has a subsolar nebular metallicity $Z = 0.05 \pm 0.02$ $Z_\odot$ (He2–O3C3 diagram; Byler et al. 2020) and (C/O) abundance ($\simeq 0.23(C/O)_\odot$). While the measured metallicity suggests a short SFH, the low (C/O) value can be explained by both an overabundance of massive O-type stars, hence, a top-heavy IMF, and a very recent burst of star formation ($<<40$ Myr).

(iv) We find a significant discrepancy between the luminosity of the UV continuum at 1500 Å and the Hβ line. Stellar models (e.g. BPASS and STARBURST99) seem to explain this tension only in the case of a young stellar population (<10 Myr) with low metallicity ($Z \simeq 10^{-4}$) and that formed following a top-heavy IMF. To some extent, the introduction of dust extinction tends to alleviate the tension even further.

(v) The Lyα emission of our target is double peaked and has a total luminosity (not corrected for extinction) of $\simeq 2 \times 10^{42}$ erg s^{-1}. The low value of the observed Lyα/Hβ ratio (Lyα/H$\beta = 2.4 \pm 0.5$) with respect to case B recombination, tends to exclude the hypothesis that the galaxy Lyα emission originates from outflows (shock heating) and gravitational cooling. This is also supported by the Lyα intrinsic EW (obtained by modelling the Lyα emission via radiative transfer 'shell-models'; e.g. Gronke & Dijkstra 2014) that is in line with the typical values in the case of star formation (i.e. 300–400 Å in modulus).

(vi) The Lyα is offset ($\delta_{Ly\alpha} \simeq 0.6$ pkpc) from the UV continuum and Balmer lines. The spatial extent of the Lyα emission is comparable to the UV continuum while it is more extended than the Balmer emission (a factor of about 2). The different extent of the emissions seems to suggest that while the UV emission traces a more extended region inhabited by an older and less extincted stellar population (10–100 Myr), the Balmer lines arise from regions of ongoing star formation ($\lesssim 10$ Myr). This could happen if phenomenon of fluorescence of Hβ and Hγ can be neglected, i.e. in the case of a low escaping fraction of ionizing radiation from the production regions of the Balmer lines. In this scenario, the Lyα extended emission would be just the consequence of resonant scattering from its region of production, an H II region.

The work presented in this paper shows the power of a multi-wavelength analysis in the characterization of galaxy properties. In particular, how the combination of rest-frame UV and optical information can help in tackling long-standing issues such as the origin of the Lyα emission within galaxies. So far, technical limitations (e.g. coarse spatial resolution, depth, and limited FoV) have significantly limited such studies to small samples of objects (e.g. Nakajima et al. 2013; Erb et al. 2016; Trainor et al. 2019; Matthee et al. 2021; Runnholm et al. 2021; Weiss et al. 2021; Pucha et al. 2022; Reddy et al. 2022). In this regard, the *James Webb Space Telescope* (*JWST*), and in particular the onboard Near-Infrared Spectrograph (NIRSpec; Jakobsen et al. 2022), will be able to extend these studies to statistical samples of galaxies at intermediate redshifts, thus possibly providing us some definitive answers.

ACKNOWLEDGEMENTS

The authors thank the anonymous referee for the useful comments and suggestions. This work is based on observations collected at the European Southern Observatory under ESO programmes 087.B-0875(A), 60.A-9195(A), and 0102.B-0741(A). This work made use of v2.2.1 of the Binary Population and Spectral Synthesis (BPASS) models as described in Eldridge et al. (2017) and Stanway & Eldridge (2018).

DATA AVAILABILITY

The data underlying this paper will be shared on reasonable request to the corresponding author.

REFERENCES

Abell G. O., 1958, ApJS, 3, 211
Ahn S.-H., Lee H.-W., 2002, J. Korean Astron. Soc., 35, 175
Allende Prieto C., Lambert D. L., Asplund M., 2001, ApJ, 556, L63
Arsenault R. et al., 2008, in Hubin N., Max C. E., Wizinowich P. L., eds, Proc. SPIE Vol. 7015, Adaptive Optics Systems. SPIE, Bellingham, p. 701524
Atek H., Furtak L. J., Oesch P., van Dokkum P., Reddy N., Contini T., Illingworth G., Wilkins S., 2022, MNRAS, 511, 4464
Bacon R. et al., 2010, in McLean I. S., Ramsay S. K., Takami H., eds, Proc. SPIE Vol. 7735, Ground-based and Airborne Instrumentation for Astronomy III. SPIE, Bellingham, p. 773508
Bacon R. et al., 2017, A&A, 608, A1
Baldwin J. A., Phillips M. M., Terlevich R., 1981, PASP, 93, 5
Berg D. A., Skillman E. D., Henry R. B. C., Erb D. K., Carigi L., 2016, ApJ, 827, 126
Berg D. A., Erb D. K., Auger M. W., Pettini M., Brammer G. B., 2018, ApJ, 859, 164
Berg D. A., Erb D. K., Henry R. B. C., Skillman E. D., McQuinn K. B. W., 2019, ApJ, 874, 93
Bonnet H. et al., 2004, in Calia D. B., Ellerbroek B. L., Ragazzoni R., eds, Proc. SPIE Vol. 5490, Advancements in Adaptive Optics. SPIE, Bellingham, p. 130
Bouwens R. J. et al., 2010, ApJ, 708, L69
Bouwens R. J., Smit R., Labbé I., Franx M., Caruana J., Oesch P., Stefanon M., Rasappu N., 2016a, ApJ, 831, 176
Bouwens R. J. et al., 2016b, ApJ, 833, 72
Bouwens R. J., Illingworth G. D., van Dokkum P. G., Oesch P. A., Stefanon M., Ribeiro B., 2022, ApJ, 927, 81
Brinchmann J., Pettini M., Charlot S., 2008, MNRAS, 385, 769
Buat V. et al., 2012, A&A, 545, A141
Bunker A. J., Moustakas L. A., Davis M., 2000, ApJ, 531, 95
Byler N., Dalcanton J. J., Conroy C., Johnson B. D., 2017, ApJ, 840, 44
Byler N., Kewley L. J., Rigby J. R., Acharyya A., Berg D. A., Bayliss M., Sharon K., 2020, ApJ, 893, 1
Calzetti D., 2013, in Falcón-Barroso J., Knapen J. H., eds, Secular Evolution of Galaxies. Cambridge Univ. Press, Cambridge, p. 419
Calzetti D., Kinney A. L., Storchi-Bergmann T., 1994, ApJ, 429, 582
Calzetti D., Armus L., Bohlin R. C., Kinney A. L., Koornneef J., Storchi-Bergmann T., 2000, ApJ, 533, 682
Caminha G. B. et al., 2016, A&A, 595, A100
Cantalupo S., Lilly S. J., Haehnelt M. G., 2012, MNRAS, 425, 1992
Carroll B. W., Ostlie D. A., 2006, An Introduction to Modern Astrophysics and Cosmology, 2nd edn. Pearson, Addison-Wesley, San Francisco
Castellano M. et al., 2012, A&A, 540, A39
Charlot S., Fall S. M., 1993, ApJ, 415, 580

Chen M. C., Chen H.-W., Gronke M., Rauch M., Broadhurst T., 2021, MNRAS, 504, 2629
Claeyssens A. et al., 2019, MNRAS, 489, 5022
Claeyssens A. et al., 2022, A&A, 666, A78
Corbin M. R., Boroson T. A., 1996, ApJS, 107, 69
Croswell K., 1996, The Alchemy of the Heavens. Oxford Univ. Press, Oxford
Dekel A., Birnboim Y., 2006, MNRAS, 368, 2
Dessauges-Zavadsky M., D'Odorico S., Schaerer D., Modigliani A., Tapken C., Vernet J., 2010, A&A, 510, A26
Dijkstra M., 2014, Publ. Astron. Soc. Aust., 31, e040
Dijkstra M., Loeb A., 2009, MNRAS, 400, 1109
Dijkstra M., Gronke M., Sobral D., 2016, ApJ, 823, 74
Dopita M. A., Sutherland R. S., 1995, ApJ, 455, 468
Eisenhauer F. et al., 2003, in Iye M., Moorwood A. F. M., eds, Proc. SPIE Vol. 4841, Instrument Design and Performance for Optical/Infrared Ground-based Telescopes. SPIE, Bellingham, p. 1548
Eldridge J. J., Stanway E. R., Xiao L., McClelland L. A. S., Taylor G., Ng M., Greis S. M. L., Bray J. C., 2017, Publ. Astron. Soc. Aust., 34, e058
Erb D. K., Pettini M., Shapley A. E., Steidel C. C., Law D. R., Reddy N. A., 2010, ApJ, 719, 1168
Erb D. K., Pettini M., Steidel C. C., Strom A. L., Rudie G. C., Trainor R. F., Shapley A. E., Reddy N. A., 2016, ApJ, 830, 52
Erb D. K., Steidel C. C., Chen Y., 2018, ApJ, 862, L10
Evans I. N. et al., 2019, Am. Astron. Soc. HEAD Meeting, #17, 114.01
Evans I. N. et al., 2020, Am. Astron. Soc. Meeting, #235, 154.05
Faisst A. L., Capak P. L., Emami N., Tacchella S., Larson K. L., 2019, ApJ, 884, 133
Faucher-Giguère C.-A., Kereš D., Dijkstra M., Hernquist L., Zaldarriaga M., 2010, ApJ, 725, 633
Feltre A., Charlot S., Gutkin J., 2016, MNRAS, 456, 3354
Fernández V., Terlevich E., Díaz A. I., Terlevich R., Rosales-Ortega F. F., 2018, MNRAS, 478, 5301
Finkelstein S. L. et al., 2011, ApJ, 729, 140
Fosbury R. A. E. et al., 2003, ApJ, 596, 797
Fusco T. et al., 2020, A&A, 635, A208
Fynbo J. U., Møller P., Thomsen B., 2001, A&A, 374, 443
Grazian A. et al., 2020, ApJ, 897, 94
Gronke M., Dijkstra M., 2014, MNRAS, 444, 1095
Gronke M., Dijkstra M., 2016, ApJ, 826, 14
Gronke M., Bull P., Dijkstra M., 2015, ApJ, 812, 123
Gronwall C., Bond N. A., Ciardullo R., Gawiser E., Altmann M., Blanc G. A., Feldmeier J. J., 2011, ApJ, 743, 9
Guo Y. et al., 2016, ApJ, 833, 37
Gutkin J., Charlot S., Bruzual G., 2016, MNRAS, 462, 1757
Hagen A. et al., 2014, ApJ, 786, 59
Hagen A. et al., 2016, ApJ, 817, 79
Haiman Z., Spaans M., Quataert E., 2000, ApJ, 537, L5
Hainline K. N., Shapley A. E., Greene J. E., Steidel C. C., 2011, ApJ, 733, 31
Hayes M., Schaerer D., Östlin G., Mas-Hesse J. M., Atek H., Kunth D., 2011, ApJ, 730, 8
Hirschmann M., Charlot S., Feltre A., Naab T., Somerville R. S., Choi E., 2019, MNRAS, 487, 333
Hoag A. et al., 2019, MNRAS, 488, 706
Humphrey A., 2019, MNRAS, 486, 2102
Humphrey A., Villar-Martín M., Vernet J., Fosbury R., di Serego Alighieri S., Binette L., 2008, MNRAS, 383, 11
Iani E. et al., 2021, MNRAS, 507, 3830
Jakobsen P. et al., 2022, A&A, 661, A80
Juneau S., Dickinson M., Alexander D. M., Salim S., 2011, ApJ, 736, 104
Kakiichi K., Gronke M., 2021, ApJ, 908, 30
Karman W. et al., 2015, A&A, 574, A11
Kashikawa N. et al., 2012, ApJ, 761, 85
Kennicutt, Robert C. J., 1998, ARA&A, 36, 189
Kereš D., Katz N., Weinberg D. H., Davé R., 2005, MNRAS, 363, 2
Kojima T., Ouchi M., Nakajima K., Shibuya T., Harikane Y., Ono Y., 2017, PASJ, 69, 44
Kong X., Charlot S., Brinchmann J., Fall S. M., 2004, MNRAS, 349, 769
Konno A., Ouchi M., Nakajima K., Duval F., Kusakabe H., Ono Y., Shimasaku K., 2016, ApJ, 823, 20
Lake E., Zheng Z., Cen R., Sadoun R., Momose R., Ouchi M., 2015, ApJ, 806, 46
Laporte N., Nakajima K., Ellis R. S., Zitrin A., Stark D. P., Mainali R., Roberts-Borsani G. W., 2017, ApJ, 851, 40
Laursen P., Sommer-Larsen J., 2007, ApJ, 657, L69
Leclercq F. et al., 2020, A&A, 635, A82
Leibundgut B. et al., 2017, The Messenger, 170, 20
Leitherer C. et al., 1999, ApJS, 123, 3
Li Z., Gronke M., 2022, MNRAS, 513, 5034
Lin Y.-H., Scarlata C., Hayes M., Feltre A., Charlot S., Bongiorno A., Väisänen P., Mogotsi M., 2022, MNRAS, 509, 489
Livermore R. C. et al., 2015, MNRAS, 450, 1812
Luridiana V., Morisset C., Shaw R. A., 2015, A&A, 573, A42
Lyman T., 1906, ApJ, 23, 181
McCarthy P. J., 1993, ARA&A, 31, 639
Mas-Ribas L., Dijkstra M., Hennawi J. F., Trenti M., Momose R., Ouchi M., 2017, ApJ, 841, 19
Matsuoka K., Nagao T., Maiolino R., Marconi A., Taniguchi Y., 2009, A&A, 503, 721
Matthee J. et al., 2021, MNRAS, 505, 1382
Meštrić U. et al., 2022, MNRAS, 516, 3532
Meurer G. R., Heckman T. M., Calzetti D., 1999, ApJ, 521, 64
Nakajima K. et al., 2012, ApJ, 745, 12
Nakajima K., Ouchi M., Shimasaku K., Hashimoto T., Ono Y., Lee J. C., 2013, ApJ, 769, 3
Nakajima K. et al., 2018, A&A, 612, A94
Nanayakkara T. et al., 2019, A&A, 624, A89
Ono Y. et al., 2010, MNRAS, 402, 1580
Orlitová I., Verhamme A., Henry A., Scarlata C., Jaskot A., Oey M. S., Schaerer D., 2018, A&A, 616, A60
Osterbrock D. E., 1962, ApJ, 135, 195
Osterbrock D. E., 1989, Astrophysics of Gaseous Nebulae and Active Galactic Nuclei. University Science Books, Sausalito, CA
Osterbrock D. E., Ferland G. J., 2006, Astrophysics of Gaseous Nebulae and Active Galactic Nuclei, 2nd edn. University Science Books, Sausalito, CA
Otí-Floranes H., Mas-Hesse J. M., Jiménez-Bailón E., Schaerer D., Hayes M., Östlin G., Atek H., Kunth D., 2012, A&A, 546, A65
Ouchi M., Ono Y., Shibuya T., 2020, ARA&A, 58, 617
Pascarelle S. M., Windhorst R. A., Keel W. C., Odewahn S. C., 1996, Nature, 383, 45
Patrício V. et al., 2016, MNRAS, 456, 4191
Peng C. Y., Ho L. C., Impey C. D., Rix H.-W., 2010, AJ, 139, 2097
Pérez-Montero E., Amorín R., 2017, MNRAS, 467, 1287
Pettini M., Steidel C. C., Adelberger K. L., Dickinson M., Giavalisco M., 2000, ApJ, 528, 96
Proxauf B., Öttl S., Kimeswenger S., 2014, A&A, 561, A10
Pucha R., Reddy N. A., Dey A., Juneau S., Lee K.-S., Prescott M. K. M., Shivaei I., Hong S., 2022, AJ, 164, 159
Reddy N. A., Erb D. K., Pettini M., Steidel C. C., Shapley A. E., 2010, ApJ, 712, 1070
Reddy N. A. et al., 2018, ApJ, 853, 56
Reddy N. A. et al., 2022, ApJ, 926, 31
Ribeiro B. et al., 2020, preprint (arXiv:2007.01322)
Rinaldi P., Caputi K. I., van Mierlo S. E., Ashby M. L. N., Caminha G. B., Iani E., 2022, ApJ, 930, 128
Runnholm A., Gronke M., Hayes M., 2021, PASP, 133, 034507
Santini P. et al., 2014, A&A, 562, A30
Schaerer D., de Barros S., Sklias P., 2013, A&A, 549, A4
Schaerer D. et al., 2022, A&A, 658, L11
Shibuya T., Ouchi M., Nakajima K., Yuma S., Hashimoto T., Shimasaku K., Mori M., Umemura M., 2014a, ApJ, 785, 64
Shibuya T. et al., 2014b, ApJ, 788, 74
Shull J. M., Jones J. R., Danforth C. W., Collins J. A., 2009, ApJ, 699, 754
Silva M., Humphrey A., Lagos P., Morais S. G., 2020, MNRAS, 495, 4707

Smit R., Swinbank A. M., Massey R., Richard J., Smail I., Kneib J. P., 2017, MNRAS, 467, 3306
Sobral D., Matthee J., 2019, A&A, 623, A157
Soto K. T., Lilly S. J., Bacon R., Richard J., Conseil S., 2016, MNRAS, 458, 3210
Stanway E. R., Eldridge J. J., 2018, MNRAS, 479, 75
Stark D. P. et al., 2014, MNRAS, 445, 3200
Steidel C. C., Strom A. L., Pettini M., Rudie G. C., Reddy N. A., Trainor R. F., 2016, ApJ, 826, 159
Ströbele S. et al., 2012, in Ellerbroek B. L., Marchetti E., Véran J.-P., eds, Proc. SPIE Vol. 8447, Adaptive Optics Systems III. SPIE, Bellingham, p. 844737
Swinbank A. M., Bower R. G., Smith G. P., Wilman R. J., Smail I., Ellis R. S., Morris S. L., Kneib J. P., 2007, MNRAS, 376, 479
Taniguchi Y. et al., 2009, ApJ, 701, 915
Trainor R. F., Strom A. L., Steidel C. C., Rudie G. C., 2016, ApJ, 832, 171
Trainor R. F., Strom A. L., Steidel C. C., Rudie G. C., Chen Y., Theios R. L., 2019, ApJ, 887, 85
Vanzella E. et al., 2016, ApJ, 821, L27
Vanzella E. et al., 2017, ApJ, 842, 47
Vanzella E. et al., 2018, MNRAS, 476, L15
Vanzella E. et al., 2020, MNRAS, 491, 1093
Veilleux S., Osterbrock D. E., 1987, ApJS, 63, 295
Veilleux S., Cecil G., Bland-Hawthorn J., 2005, ARA&A, 43, 769
Verhamme A., Schaerer D., Maselli A., 2006, A&A, 460, 397
Verhamme A., Dubois Y., Blaizot J., Garel T., Bacon R., Devriendt J., Guiderdoni B., Slyz A., 2012, A&A, 546, A111
Vernet J., Fosbury R. A. E., Villar-Martín M., Cohen M. H., Cimatti A., di Serego Alighieri S., Goodrich R. W., 2001, A&A, 366, 7
Weilbacher P. M., Streicher O., Urrutia T., Jarno A., Pécontal-Rousset A., Bacon R., Böhm P., 2012, in Radziwill N. M., Chiozzi G., eds, Proc. SPIE Vol. 8451, Software and Cyberinfrastructure for Astronomy II. SPIE, Bellingham, p. 84510B
Weilbacher P. M., Streicher O., Urrutia T., Pécontal-Rousset A., Jarno A., Bacon R., 2014, in Manset N., Forshay P., eds, ASP Conf. Ser. Vol. 485, Astronomical Data Analysis Software and Systems XXIII. Astron. Soc. Pac., San Francisco, p. 451
Weiss L. H. et al., 2021, ApJ, 912, 100
Yang Y., Zabludoff A. I., Davé R., Eisenstein D. J., Pinto P. A., Katz N., Weinberg D. H., Barton E. J., 2006, ApJ, 640, 539
Zanella A. et al., 2015, Nature, 521, 54
Zeimann G. R. et al., 2015, ApJ, 814, 162
Zheng Z., Wallace J., 2014, ApJ, 794, 116

APPENDIX A: DETECTION OF ADDITIONAL LYα EMITTERS

During the analysis of the MUSE data set in our hands, we detected five LAEs in addition to our target and the already known system at $z \sim 3.4$ (e.g. Livermore et al. 2015; Iani et al. 2021). Among the newly discovered sources, we found two multiply-imaged systems (at $z \simeq 4.65$ and $z \simeq 4.92$), and three single-imaged LAEs (at $z \simeq 4.57$ and $z \simeq 4.92$). According to the shape of their Lyα emission and their spatial position, we exclude the hypothesis that the single-imaged LAEs at $z \simeq 4.92$ are additional images of the multiply-imaged system at the same redshift. In Table A1, we provide the spatial coordinates of these targets and a rough estimate of their redshift. For the nomenclature of these targets, we follow the naming adopted by Livermore et al. (2015). We present MUSE cutouts for the Lyα and UV continuum emission of each new target and related multiple images, as well as a zoomed-in image of their UV spectrum around the Lyα line.

Table A1. Approximate redshift and spatial coordinates of the LAEs serendipitously detected in the MUSE observations of the A2895 galaxy cluster. We also report the possible presence of a possible counterpart in the available *HST* ACS/WFC F606W image.

LAE	z	M1	M2	M3	*HST* detected
		$\alpha_{J2000.0}$, $\delta_{J2000.0}$	$\alpha_{J2000.0}$, $\delta_{J2000.0}$	$\alpha_{J2000.0}$, $\delta_{J2000.0}$	
A2895a	3.395	01:18:11.190, −26:58:04.40	01:18:10.890, −26:58:07.50	01:18:10.570, −26:58:20.50	Yes
A2895b	3.721	01:18:11.127, −26:57:59.36	01:18:10.543, −26:58:10.56	01:18:10.439, −26:58:14.36	Yes
A2895c	4.57	01:18:09.151, −26:57:47.82	–	–	No
A2895d	4.65	01:18:11.127, −26:57:59.56	01:18:10.304, −26:58:10.96	–	No
A2895e	4.92	01:18:10.887, −26:57:58.56	01:18:10.783, −26:57:58.96	01:18:10.319, −26:58:08.36	No
A2895f	4.92	01:18:09.465, −26:57:51.82	–	–	No
A2895g	4.92	01:18:12.532, −26:58:38.82	–	–	No

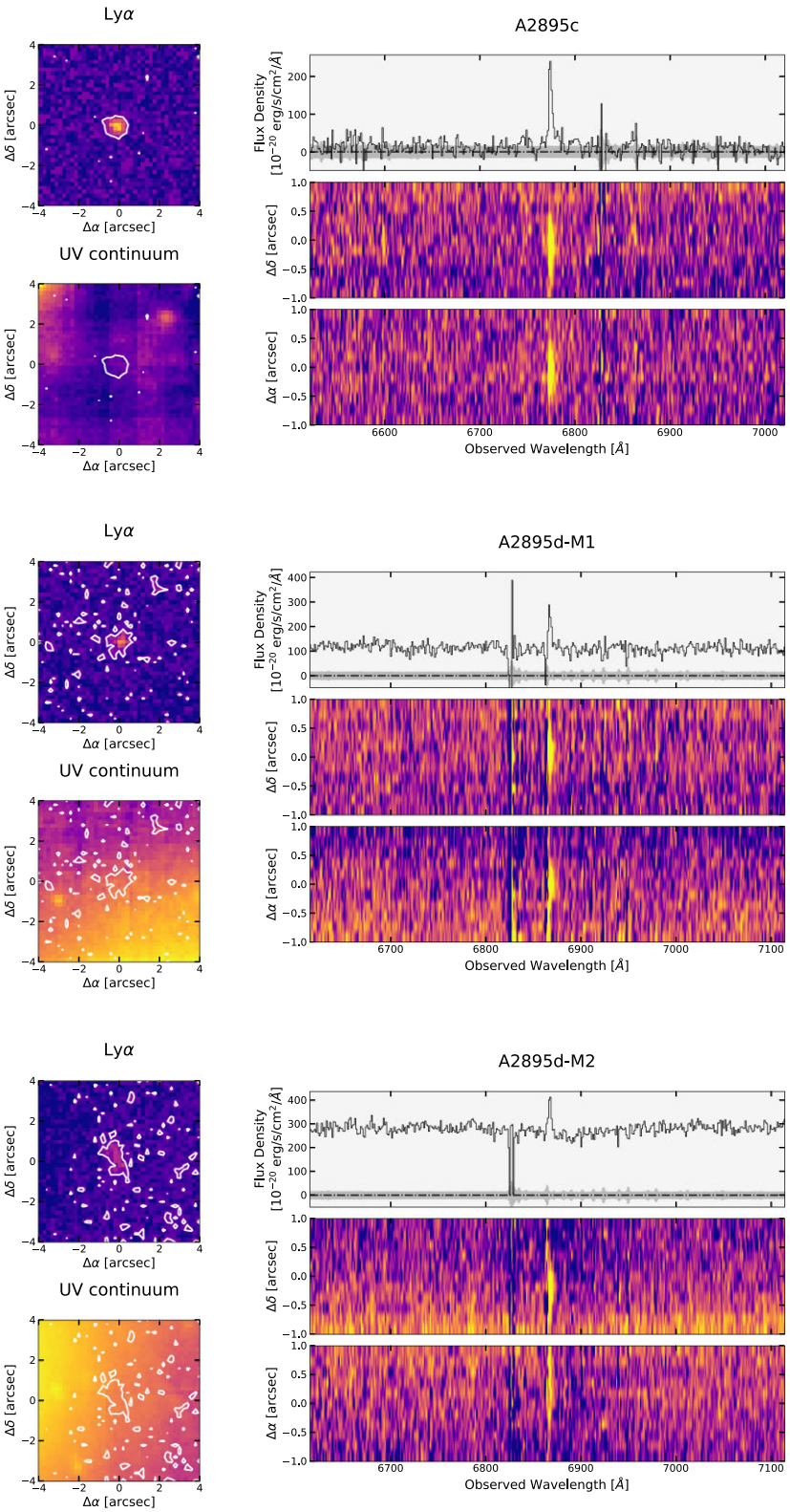

Figure A1. Cutout images and spectra for the five serendipitously detected LAEs in Abell 2895 (see Table A1). The left hand side panels show the pseudo-narrow band image of the targets' Lyα emission (top) and their UV continuum emission (bottom). The UV continuum images are not decontaminated by bright neighbours. The right hand side panels present the targets' UV spectrum in a wavelength window ($\pm$250Å) centred at the position of the observed Lyα emission. On top, we present the targets' 1D spectrum (in black) with the grey-shadowed area representative of the 1σ error. The central and bottom panels show the 2D spectra obtained by collapsing the MUSE datacube along the right ascension and declination axis, respectively.

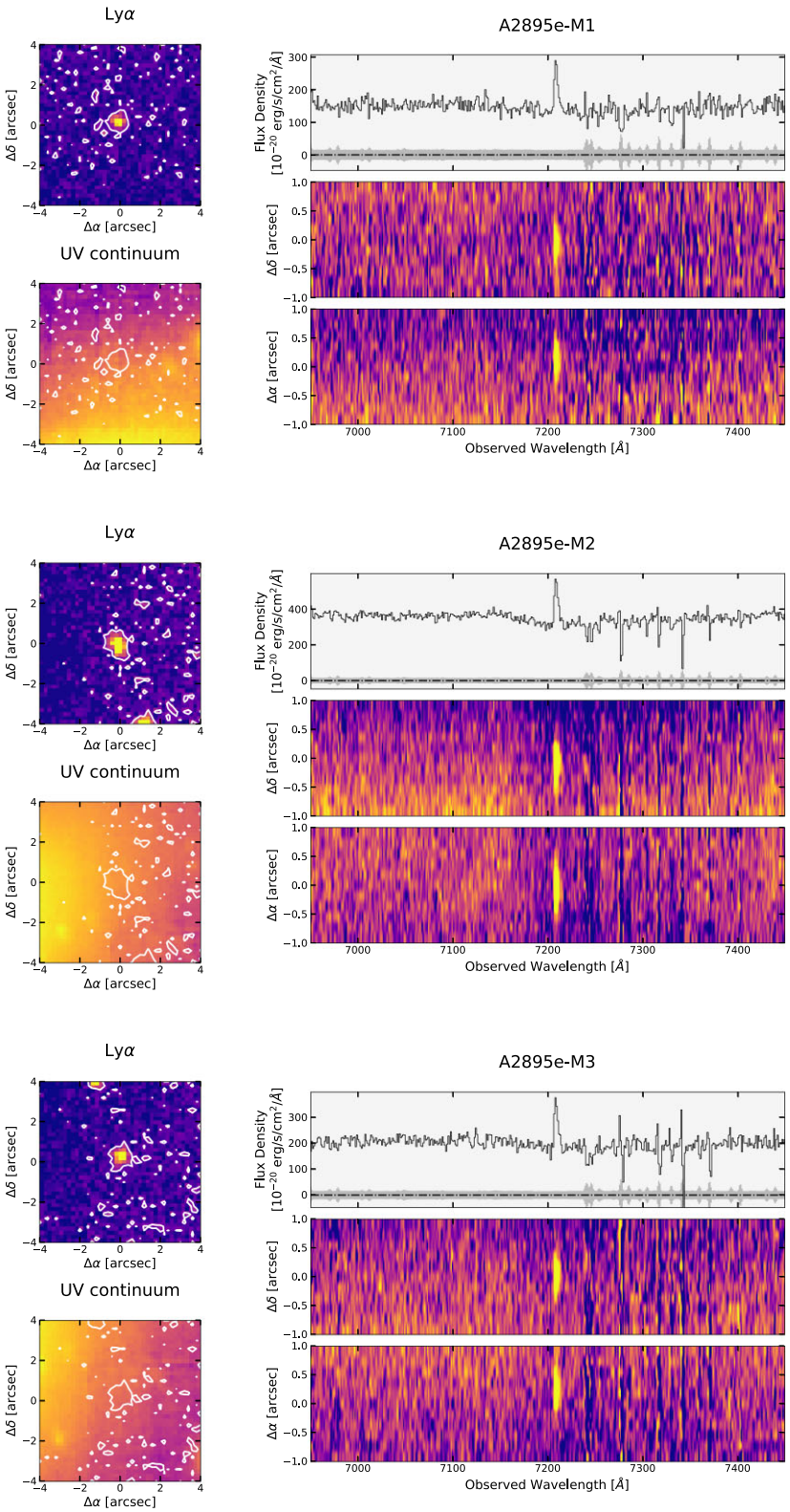

Figure A1. *Continued.*

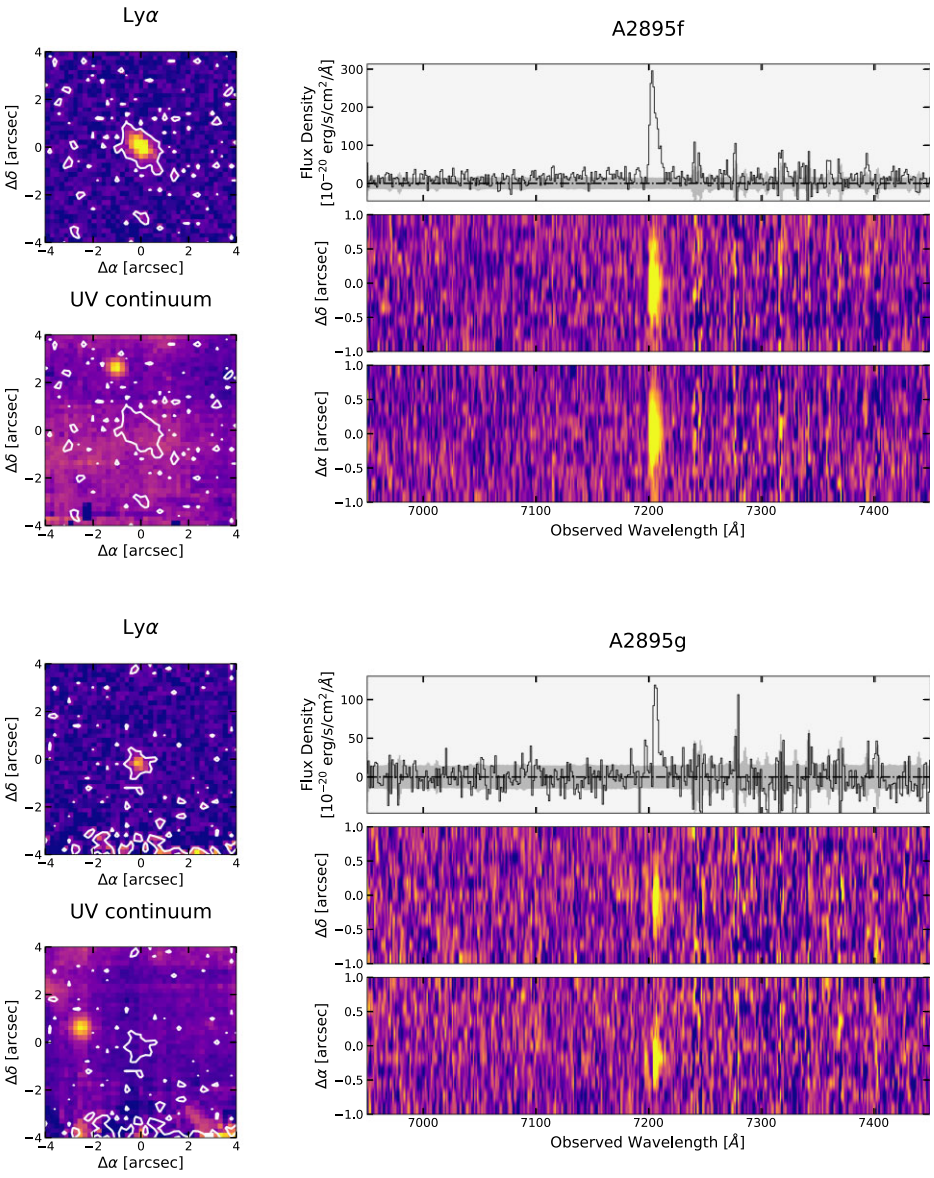

Figure A1. *Continued.*

This paper has been typeset from a TEX/LATEX file prepared by the author.